https://doi.org/10.5194/egusphere-2026-939
Preprint. Discussion started: 8 May 2026

Sensitivity of CO_2 exchange in WRF-VPRM to model resolution and parameter settings over Alpine topography

Matthias Reif[1], Mathias W. Rotach[1], Georg Wohlfahrt[2], and Alexander Gohm[1]

[1]Universität Innsbruck, Institut für Atmosphären- und Kryosphärenwissenschaften, Austria
[2]Universität Innsbruck, Institut für Ökologie, Austria

Correspondence: Matthias Reif (matthias.reif@posteo.de)

Abstract. As the terrestrial carbon sink remains the most uncertain component of the global CO_2 budget, systematic misrepresentation of biospheric CO_2 exchange in complex mountainous regions limits the reliability of climate projections. This study employs the Vegetation Photosynthesis and Respiration Model coupled to the Weather Research and Forecasting model (WRF-VPRM) in real-case simulations over the European Alps. It investigates whether Alpine CO_2 exchange is appropriately represented when using default or regionally optimized VPRM parameters, quantifies the sensitivity of modelled CO_2 exchange to horizontal grid spacing at scales typical for global weather prediction (9 km) and climate models (54 km), and identifies the physical drivers of resolution-induced biases. Simulations with coarser horizontal grid spacing are compared with a regional-scale 1 km reference. Throughout 2012, 12 clear-sky and 12 cloudy/rainy days are simulated using three different VPRM parameter sets: default European (DF), Alpine-optimized (ALPS), and site-specific (SITE).

Validation against five Alpine FLUXNET sites indicates that the SITE parameters perform best overall. The ALPS configuration provides a nearly unbiased representation of ecosystem respiration (R_{eco}) but overestimates gross primary production (GPP), whereas the DF configuration strongly underestimates both R_{eco} and GPP. In DF, these biases partially compensate, resulting in comparatively good performance for net ecosystem exchange (NEE) despite physically inconsistent flux components.

Systematic biases in CO2 uptake and their magnitude depend on grid spacing and prevailing meteorological conditions. Resolution-induced biases in NEE (relative to 1 km simulations) under clear-sky conditions decrease from several percent (7% for ALPS, 4% for DF) at 9 km to near zero at 54 km. For clear sky, coarser resolutions yield higher net CO2 uptake. In contrast, under cloudy and rainy conditions coarse grids have lower simulated uptake than at 1 km, while the biases substantially increase (from order 10% at 9 km grid spacing to over 40% at 54 km). If yearly NEE is estimated from 12 days each for clear-sky and cloudy/rainy conditions, differences due to resolution are minimal at 9 km , while differences due to the parameter set (ALPS vs. DF) amount to 15%. At 54 km grid spacing, resolution effects for both ALPS (17%) and DF (13%) exceed parameter effects (8%). Taken together, the results imply that resolution-induced errors govern annual NEE uncertainty at coarse resolution (O(100 km)), but at finer resolutions (O(10 km)) the relative impact of parameter optimization dominates.

Analytical estimates based on temperature derivatives indicate that 35–42% of the differences in GPP and 71–85% in R_{eco} differences between resolutions can be attributed directly to temperature. Additionally, a linear perturbation analysis confirms

https://doi.org/10.5194/egusphere-2026-939
Preprint. Discussion started: 8 May 2026

the key role of temperature in unresolved topography, while it clarifies that radiation accounts for most of the remaining GPP variance and that e.g. water stress and vegetation types from satellite data add smaller but systematic biases.

1 Introduction

The terrestrial carbon sink has the largest quantified uncertainty among the main terms in the global carbon budget (Friedlingstein et al., 2020). Process models estimate the residual mismatch between sources and sinks, expressed as the budget imbalance, representing the difference between natural (oceanic and terrestrial) fluxes and anthropogenic emissions. Terrestrial ecosystem sinks respond in different ways to rising temperature and CO_2 through carbon-nitrogen interactions and CO_2 fertilization (Zaehle and Dalmonech, 2011). Furthermore, Kattge and Knorr (2007) documented that photosynthesis or gross primary production (GPP) typically increases with temperature up to a plant-specific optimum (T_{opt}). Beyond T_{opt} photosynthetic efficiency declines and acclimates to ambient temperatures and humidity by closing its stomata, resulting in a bell-shaped temperature response. At the ecosystem level, Liu (2020) confirmed that T_{opt} acclimates on daily to seasonal timescales while it lags behind warming, but uptake declines once ambient temperature exceeds this limit. Uncertainties in CO_2 fertilization, acclimation processes, and their complex interactions limit the reliability of modeled carbon-climate feedback. Consequently, climate projections retain only medium confidence regarding terrestrial carbon sink responses (Fatichi et al., 2019; Walker et al., 2021).

High-quality observational data are essential for evaluating biospheric fluxes of CO_2. FLUXNET provides a global, standardized network of eddy covariance measurements that serves as a benchmark for evaluating and tuning terrestrial biosphere models (Friend et al., 2007). The FLUXNET2015 dataset, processed via the ONEFlux pipeline, is widely used to constrain model parameters and assess performance across diverse ecosystems (Pastorello et al., 2020). In Europe, FLUXNET2015 covers the period 1996 to 2014, with highest data availability around the Alps in 2012.

In mountainous terrain, systematic nighttime flux biases caused by advection and storage under low-turbulence conditions limit measurement reliability, as eddy covariance systems commonly underestimate respiration when CO_2 advection is not captured under stable stratification (Aubinet et al., 2010). Yet, direct measurements of advective fluxes have not resolved this issue, as they frequently exhibit weak coherence with the expected carbon fluxes. To mitigate these biases, Platter et al. (2024) recommended applying multiple filtering strategies, including traditional friction velocity (u_*) filtering and newer methods incorporating stability metrics and physically based measures of flow decoupling.

Complementary to the evaluation of site-level measurements, the Copernicus Atmosphere Monitoring Service (CAMS) provides global forecasts of atmospheric concentrations and surface CO_2 exchange using a hybrid modeling approach (Inness et al., 2019). Biospheric CO_2 fluxes are simulated online by the process-based CHTESSEL model within the ECMWF Integrated Forecasting System (IFS), ensuring physical consistency with evapotranspiration (Boussetta et al., 2013). Seasonal and annual flux biases are corrected by the Biogenic Flux Adjustment Scheme (BFAS), which assimilates atmospheric CO_2 observations to constrain the land sink (Agustí-Panareda et al., 2016). This top-down correction addresses structural errors in the land surface model and improves global carbon budget closure. However, CAMS still exhibits spatially varying biases over

https://doi.org/10.5194/egusphere-2026-939
Preprint. Discussion started: 8 May 2026

continental regions, particularly in areas dominated by strong anthropogenic or biogenic fluxes of CO_2 (Chen et al., 2019). While it well reproduces the trend in the global atmospheric CO_2 concentration, performance varies regionally and in the seasonal cycle due to ecosystem-specific flux dynamics (Custódio et al., 2022).

In addition, the horizontal grid spacing of the operational IFS/CAMS configuration (approximately 9-10 km) is insufficient to resolve complex topography such as the Alpine terrain and associated valley circulations, whereas simulations at 1 km grid spacing show substantially improved performance when evaluated against large-eddy simulations at 50 m grid spacing (Wagner et al., 2014b). Furthermore, grid spacings above around 4 km cannot explicitly resolve deep convection and cumulus parameterization schemes have to be applied, potentially introducing systematic biases in atmospheric transport and mixing (Prein et al., 2015).

Accurate representation of ecosystem vegetation through plant functional types (PFT) is crucial for simulating ground-based and atmospheric datasets with land surface models (Woude et al., 2023; de Bode et al., 2023). The CORINE 2018 Land Cover dataset (European Union's Copernicus Land Monitoring Service information, 2020) provides a detailed 100 m × 100 m land cover and land use map for Europe, categorized into 44 distinct classes. Although its spatial coverage is limited to Europe, it offers substantial improvements over coarser global products and represents the most consistent and appropriate choice for high-resolution meteorological and ecosystem modeling for Europe. Woude et al. (2023) present the downscaling of coarser flux models, such as the Simple Biosphere Model Version 4 (SiB4) at 0.5°×0.5° grid size and the CarbonTracker Europe High-Resolution (CTE-HR) product at 0.1°×0.2° grid spacing, thereby introducing subgrid biospheric carbon exchange. This is a crucial development because land-use differences often dominate over meteorological variability, which Woude et al. (2023) validate by the strong spatial correlation between downscaled CO_2 fluxes and observed gradients.

The P-model (Wang et al., 2017b; Stocker et al., 2020; Mengoli et al., 2022) is a light-use efficiency model rooted in eco-evolutionary optimality theory, designed to simulate GPP with minimal empirical parameterization. One key strength of the P-model is its representation of photosynthetic acclimation to environmental drivers (e.g., light, temperature, vapor pressure deficit, CO_2) and its independence from PFTs, which allows it to dynamically adjust photosynthetic capacity over timescales of weeks to months to any ecosystem. This characteristic makes the P-model particularly suitable for investigating physiological acclimation in mountainous terrain, where diverse climate zones coexist over short distances. In the present study, the P-model is not applied but introduced to highlight its potential for simulating acclimation processes in the discussion. However, Mengoli et al. (2022) point out that the P-model has limitations in representing adjustment to soil moisture stress and to cold conditions in spring, which can lead to GPP overestimations in spring and arid regions. Although recent work has introduced a promising soil moisture stress function, interactive coupling of transpiration and GPP in dynamic model environments remains a challenge (Mengoli et al., 2025).

The Vegetation Photosynthesis Respiration Model (VPRM) coupled to the Weather Research and Forecasting (WRF) model (Mahadevan et al., 2008; Beck et al., 2011; Chen et al., 2019), here named WRF-VPRM, is a diagnostic light-use efficiency model which calculates biogenic surface fluxes online, while treating atmospheric CO_2, CH_4 and CO as passive tracers. VPRM computations use shortwave radiation, and near-surface air temperature simulated by WRF and satellite-derived vegetation indices as input. The enhanced vegetation index (EVI) and land surface water index (LSWI) can be derived from MODIS

https://doi.org/10.5194/egusphere-2026-939
Preprint. Discussion started: 8 May 2026

reflectance data (MOD09A1, Version 6), which are available in 8-day intervals. To ensure continuity for the VPRM in the post-MODIS era, Glauch et al. (2025) developed pyVPRM, a modular Python-based framework that integrates globally available, contemporary satellite products from Sentinel-2 and VIIRS, along with high-resolution, dynamic land cover maps like the Copernicus Dynamic Land Cover Collection 3. In conjunction with land cover maps, the integration of high-resolution (20 m) Sentinel-2 data particularly improves flux estimates for heterogeneous landscapes like croplands and grasslands due to better resolving the flux footprint.

In general, coarse-resolution models smooth or average topography, suppressing slope-valley structure and associated mesoscale circulations (Wagner et al., 2014a). This simplification alters near-surface temperature and vapor pressure deficit (VPD) and thus biases the environmental drivers of biospheric CO_2 fluxes compared to high-resolution simulations. Because biospheric fluxes respond nonlinearly to temperature and humidity, complex terrain with its strong spatial heterogeneity in thermal, radiative, and land-surface conditions amplifies resolution-dependent discrepancies. Consequently, temperature-driven differences in GPP between coarse and fine resolutions are spatially non-uniform and cannot be adequately addressed through a simple bias correction. Their sign and magnitude depend on whether ambient temperature lies above or below T_{opt}. Capturing these processes is essential for representing biospheric CO_2 fluxes in complex topography. Moreover, coarse grids represent land-surface characteristics as spatial averages of satellite data and PFT, whereas high-resolution models capture the heterogeneous land-cover mosaic. As a result, coarse models apply biased temperatures to biophysical models using inappropriate PFT information.

This study addresses the misrepresentation of CO_2 fluxes in climate models arising from complex topography, which, depending on the definition, affects more than 50% of the global land surface (Rotach et al., 2014). Rotach et al. (2014) presume that traditional carbon exchange models, often developed for flat terrain, systematically misrepresent net CO_2 exchange in complex topography. It is argued that coarse-resolution models fail to resolve significant surface exchange processes. Consequently, the paper emphasizes the need for subgrid-scale parameterizations to accurately represent these terrain-induced effects on CO_2 exchange in atmospheric models, drawing a parallel to existing subgrid-scale orographic drag parameterizations for momentum. Cao et al. (2025) quantify terrain-induced changes in the projection of solar radiation and of land surface properties from satellite data, affecting mass and energy fluxes, particularly GPP and evapotranspiration (ET). The importance of CO_2 exchange in complex terrain highlights the need for further study, since plants respond instantaneously and through acclimation to altitude-specific microclimates differing in temperature, humidity, and CO_2 from coarse model representations.

Reif et al. (2024) conducted ensemble simulations of an idealized valley at 1 km grid size under clear-sky conditions compared to flat reference simulations at 40 km. The idealized valley exhibits on average cooler vegetation temperatures and lower vapor pressure deficit during daytime conditions compared to the coarse-grid simulation, leading to enhanced daytime CO_2 uptake. In contrast, nocturnal conditions in the valley are characterized by warmer temperatures, which enhance R_{eco} and result in increased CO_2 emissions relative to the coarse-grid representation. Over 24 h, the opposing day- and nighttime fluxes yield a stronger net CO_2 uptake in the valley of 0.18 gC m^{-2} day^{-1}, corresponding to 12% of the daily total of -1.5 gC m^{-2} day^{-1} (equivalent to a daily mean flux of -1.45 μmol m^{-2} s^{-1}). The open questions after this ideal-terrain study are: the extent to which these findings are valid in real-case simulations of topographic and land-cover heterogeneity, how robust they are

https://doi.org/10.5194/egusphere-2026-939
Preprint. Discussion started: 8 May 2026

across different biospheric models and parameter specifications, and whether subgrid flux variability can be represented in coarse-scale models by a parameterization.

Building on these questions, the present study advances from idealized valleys to real-case simulations in complex terrain. We address the following questions:

1. How does horizontal grid spacing at O(10 km) and O(100 km) affect CO_2 exchange over the Alps compared to a regional O(1 km) reference?
2. What is the sensitivity of simulated CO_2 fluxes to VPRM parameter choice? Do default European or Alpine-optimized parameters adequately represent biospheric exchange in complex terrain?
3. How well do the 1 km simulations reproduce CO_2 fluxes at Alpine FLUXNET sites, and how do they compare to the CAMS reanalysis product?
4. Which physical drivers, temperature, radiation, and satellite-derived vegetation indices, explain the unresolved CO_2 flux variance at coarse grid spacing?
5. Is a subgrid-scale parameterization of biospheric CO_2 exchange feasible and warranted?

2 Methods and model design

2.1 General WRF setup

In this study, the performance of WRF-VPRM over complex mountainous terrain is studied in an 'extended case study' approach. Single days (the classic case study) cannot reproduce the variability due to ambient conditions and climate time-scales require excessive computing resources, in particular if different resolutions and parameter settings are to be tested (see below). A representative sample of 24 days of simulations throughout the year 2012, one clear-sky and one cloudy/rainy day for each month, respectively, were chosen to cover a seasonal cycle and to have a minimum sample size that allows for basic statistical conclusions.

WRF-VPRM was applied here to simulate regional meteorology and biogenic CO_2 fluxes in the European Alps. VPRM was chosen for its simplicity, computational efficiency, and wide application in WRF, making VPRM particularly suitable for regional-scale studies (e.g. Segura-Barrero et al., 2025; Jose et al., 2025; Zhao et al., 2023; Huggannavar and Indu, 2023; Raju et al., 2023; Parazoo et al., 2022; Callewaert et al., 2022; Gourdji et al., 2022). The study region (Fig. 1) is characterized by complex Alpine topography. In total, simulations are presented at 3 different grid spacings. The domains with the coarsest (d01, 54 km) and the intermediate grid spacing (d02, 9 km) have the same size, while the nested domain (d03) is at 1 km horizontal grid spacing. An intermediate 3 km domain has the same size as the 9 km domain to drive the 1 km grid, however, data from the 3 km grid was excluded from the analysis.

Simulations were conducted using ERA5 reanalysis (Hersbach et al., 2023) at 0.25°×0.25° grid spacing as initial and boundary conditions of meteorological fields, interpolated on 81 vertical eta-levels in WRF. For elevation Shuttle Radar Topography

https://doi.org/10.5194/egusphere-2026-939
Preprint. Discussion started: 8 May 2026

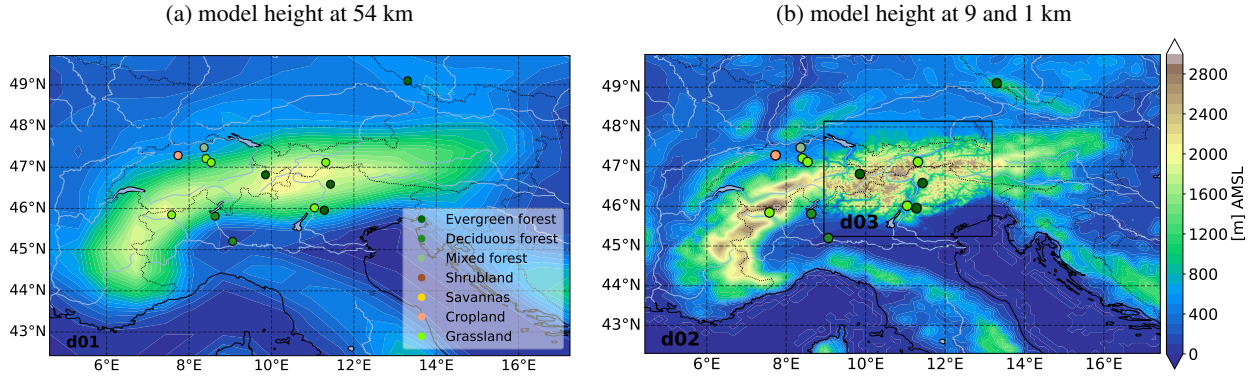

Figure 1. Contours of WRF topography for the study domains. Panel (a) shows domain d01 at 54 km horizontal grid spacing. Panel (b) shows domains d02 (9 km grid spacing) and the nested domain d03 (1 km grid spacing). The locations of the FLUXNET sites used for ALPS parameter optimization are marked by their respective PFT color (legend in a), there are no FLUXNET sites in the domains for shrubland and savanna.

Mission (SRTM) data at 3-arc-second grid spacing (JPL, 2013) was applied, which corresponds to about 90 m in our target area. Each run started at 18:00 UTC and covered 30 h including a 6 h spin-up. Land cover was prescribed from CORINE following the method of de Bode et al. (2023) who define new WRF tables of the physical properties for each category which enables high-resolution, region-specific land-use representation. Biogenic CO_2 fluxes were simulated with VPRM applying default and custom parameter settings in parallel. Input from satellite data (EVI, LSWI and CORINE) for VPRM was converted using the VPRM preprocessor tool within pyVPRM (Glauch et al., 2025).

Land cover from CORINE was used consistently in both the Noah land surface scheme within WRF (Chen and Dudhia, 2001) and in VPRM, where CORINE classes are mapped to plant functional types (PFT) of VPRM. The CORINE to VPRM mapping (Table D1 in Appendix D) shows that VPRM types may combine several CORINE vegetation classes with distinct biophysical properties. Deciduous broadleaf forest (DBF) and evergreen needleleaf forest (ENF) correspond one-to-one, implying identical thermal conditions between the CORINE classes and the VPRM PFT. In contrast, mixed forest (MF) and grassland (GRA) each aggregate two different CORINE classes, leading to differences in surface energy and water fluxes (de Bode et al., 2023). Cropland (CRO) represents an even broader aggregation, combining ten CORINE categories into a single VPRM type, thus reflecting diverse underlying thermal regimes.

Figure 2(a) illustrates the representation of dominant vegetation types of d01 interpolated on the inner domain d03, where the fractional contributions of PFT within each coarse grid cell are visualized by pie charts. These fractions are derived from the high-resolution land cover and allow for a subgrid mixture of PFTs in VPRM. To reduce boundary-related artifacts, the outermost ten grid-points along each lateral boundary in d03 were discarded (Marbaix et al., 2003), also interpolated results from d01 and d02 were analyzed only for the remaining interior domain.

To better represent subgrid heterogeneity and terrain-atmosphere interactions, slope radiation correction, topographic shading and the surface mosaic option of the Noah land surface model were activated in WRF. In addition, solar zenith angle

https://doi.org/10.5194/egusphere-2026-939
Preprint. Discussion started: 8 May 2026

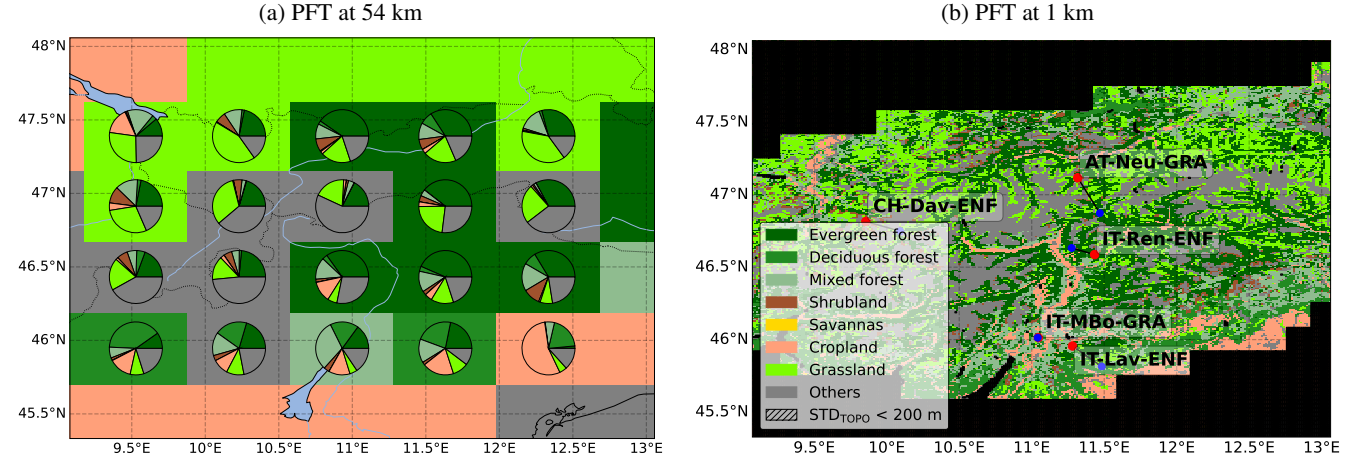

Figure 2. Representation of plant functional types (PFT) and FLUXNET site locations. Panel (a) shows the dominant vegetation types of the 54 km grid (d01) interpolated onto the inner domain (d03), overlaid with pie charts indicating the subgrid PFT mix. Panel (b) shows dominant vegetation types of the 1 km grid (d03). Red dots indicate the physical FLUXNET site locations, blue dots indicate the nearest representative grid-points selected for validation, which were chosen within a 30 km radius to minimize differences in height (< 100m), aspect ($\leq 20°$), and slope ($\leq 10°$) relative to the actual site. Areas with a standard deviation of subgrid-scale topography of STD_{TOPO} < 200 m and over water are hatched as they are not used in the evaluations.

interpolation between radiation calls was activated, accordingly shortwave radiation follows the cosine of the solar zenith angle at every model timestep rather than being held constant over the radiation interval (Morcrette, 2000). This is equivalent to the daylight-mean cosine approach implemented in established climate model radiation schemes, where shortwave fluxes are weighted by the ratio of the instantaneous to the interval-mean cosine of the solar zenith angle at each model timestep (Hogan and Bozzo, 2018). Since global climate models typically employ radiation call intervals of approximately 1 h (Bonnet et al., 2025), this correction ensures a consistent treatment of solar zenith angle and is required for a fair comparison of resolution-dependent radiation effects.

The energy balance in WRF-Noah without the mosaic option would be solved only for the dominant vegetation type or PFT within a grid cell, the mosaic or tile approach subdivides each grid cell into N tiles of distinct land cover categories (here 5 tiles of CORINE categories). Surface fluxes and state variables are computed for each tile and subsequently aggregated, with grid-cell averaged temperature weighted to conserve outgoing longwave radiation (Li et al., 2013). This treatment of subgrid heterogeneity yields a more realistic near-surface temperature compared to single-category assignments, reducing systematic bias in surface temperature simulations.

At 1 km grid spacing (in d03), the distribution of dominant PFT as represented in VPRM are shown in Fig. 2b, together with the physical locations of FLUXNET sites and their nearest representative grid-points, which were used for validation (see Sect. 3.1). To confine the analysis to mountainous or topographically complex terrain, flat areas were excluded using the subgrid-scale topographic standard deviation (STD_{TOPO}) derived from the 1 km grid with underlying SRTM (90 m) data.

https://doi.org/10.5194/egusphere-2026-939
Preprint. Discussion started: 8 May 2026

A threshold of 200 m was applied because grid cells with STD_{TOPO} < 200 m exhibit only weak sensitivity to subgrid orographic variability (not shown), and including these flatter areas would dilute the amplitude of domain-mean signals. This threshold therefore isolates grid cells with pronounced subgrid variability and effectively masks out the low-lying regions (< 500 m AMSL) present in d03. Mean diurnal cycles were derived from hourly averages over 12 clear-sky and 12 cloudy/rainy days in 2012. Clear-sky days were identified for each month from the GFS archive as 24-hour periods with nearly cloud-free conditions over domain d01, whereas cloudy/rainy days corresponded to mostly full cloud cover with varying amounts of precipitation.

2.2 VPRM model equations

In general, net ecosystem exchange (NEE) of CO_2 represents the balance between ecosystem respiration (R_{eco}), releasing CO_2, and gross primary production (GPP), denoting photosynthetic CO_2 uptake, with

$$\mathrm{NEE} = \mathrm{R_{eco}} - \mathrm{GPP}. \tag{1}$$

Here, GPP is defined as a positive flux and is therefore subtracted from R_{eco}. In VPRM the sum of GPP over eight PFT is defined as

$$\mathrm{GPP} = \sum_{v}^{\mathrm{N_{PFT}}} \lambda_v \, T_{\mathrm{scale},v} \, P_{\mathrm{scale},v} \, W_{\mathrm{scale},v} \, \mathrm{RAD}_v \mathrm{EVI}_v \, \mathrm{veg}_{\mathrm{frac},v}, \qquad v \in \{\mathrm{ENF, DBF, MF, SHB, SAV, CRO, GRA, OTH}\} \tag{2}$$

for each vegetation fraction $\mathrm{veg}_{\mathrm{frac},v}$, where the subscript v indicates the respective PFT. The abbreviations in the list for v stand for evergreen needleleaf forest (ENF - here named evergreen forest), deciduous broadleaf forest (DBF - here named broadleaf forest), mixed forest (MF), shrubland (SHB), savanna (SAV), cropland (CRO), grassland (GRA) and others (OTH). λ_v is the potential light-use efficiency, and $T_{\mathrm{scale},v}$, $P_{\mathrm{scale},v}$, and $W_{\mathrm{scale},v}$ are dimensionless scaling factors (0-1) representing temperature, phenology, and water stress, respectively. RAD_v is the irradiance contribution, as defined below. The enhanced vegetation index (EVI) is obtained from MODIS remote sensing products, the term $\mathrm{RAD}_v\mathrm{EVI}_v$ approximates the radiation absorbed for photosynthesis.

Eddy covariance flux sites typically provide simultaneous measurements of photosynthetically active radiation (PAR), whereas numerical weather prediction (NWP) models and associated analysis or reanalysis products generally lack this variable. Consequently, VPRM parameter optimization must either rely on NWP derived shortwave downward radiation (S↓) or on S↓ converted to PAR. The original formulation of VPRM by Mahadevan et al. (2008) converts S↓ to PAR using the empirical relation $\mathrm{PAR} \approx \mathrm{S}\downarrow/0.505$, as also explicitly defined in several recent studies (e.g. Li et al., 2020; Park et al., 2020; Hu et al., 2020; Raju et al., 2023; Glauch et al., 2025). In contrast, the standard WRF implementation of VPRM uses S↓ (i.e., PAR = S↓) directly to approximate PAR, an approach applied by Beck et al. (2011) and Gerbig (2024). To enable using the WRF-VPRM European default parameters as a reference, here the Alpine parameter sets were optimized under the PAR = S↓ assumption (see Sect. 2.2.1). S↓ from WRF is used directly but with a unit conversion from W m^{-2} to μmol m^{-2} s^{-1} to approximate PAR.

https://doi.org/10.5194/egusphere-2026-939
Preprint. Discussion started: 8 May 2026

The irradiance contribution is then computed as

$$\mathrm{RAD}_v = \frac{\mathrm{S}\downarrow}{1 + \frac{\mathrm{S}\downarrow}{\mathrm{PAR}_{0,v}}}, \tag{3}$$

where the term $\frac{1}{1+\frac{\mathrm{S}\downarrow}{\mathrm{PAR}_{0,v}}}$ is a dimensionless scaling factor describing the saturation of photosynthetic activity due to irradiance, with $\mathrm{PAR}_{0,v}$ (μmol m^{-2} s^{-1}) as the half-saturation value. $\mathrm{PAR}_{0,v}$ is PFT dependent and has to be regionally calibrated with measurements, which was done here by directly optimizing $\mathrm{PAR}_{0,v}$ against S$\downarrow$ from FLUXNET for each PFT.

The temperature scaling function is

$$T_{\mathrm{scale},v} = \frac{(T_{2\mathrm{m}} - T_{\mathrm{min},v})(T_{2\mathrm{m}} - T_{\mathrm{max},v})}{(T_{2\mathrm{m}} - T_{\mathrm{min},v})(T_{2\mathrm{m}} - T_{\mathrm{max},v}) - (T_{2\mathrm{m}} - T_{\mathrm{opt},v})^2}, \tag{4}$$

where the 2 m air temperature ($T_{2\mathrm{m}}$) is similar for all PFT but the minimum temperature ($T_{\mathrm{min},v}$) and the maximum temperature ($T_{\mathrm{max},v}$) are dependent on the respective PFT. Identical to the default implementation of WRF-VPRM, GPP was set to zero below $T_{\mathrm{min},v}$ (0 to 5 °C) and above $T_{\mathrm{max},v}$ (40 °C), reflecting photosynthetic thresholds of PFT. The optimum temperature (T_{opt}) indicates the temperature of maximum photosynthetic efficiency, its calculation is described in detail in Sect. 2.2.2.

Phenology is represented by

$$\mathrm{P}_{\mathrm{scale},v} = \frac{1 + \mathrm{LSWI}_v}{2}, \tag{5}$$

and water stress by

$$\mathrm{W}_{\mathrm{scale},v} = \frac{1 + \mathrm{LSWI}_v}{1 + \mathrm{LSWI}_{\mathrm{max},v}}, \tag{6}$$

where LSWI is the Land Surface Water Index derived from MODIS bands 2 and 6 (Chandrasekar et al., 2010), and $\mathrm{LSWI}_{\mathrm{max}}$ denotes the maximum daily LSWI during May-October based on multi-year means (Xiao et al., 2011).

$\mathrm{R}_{\mathrm{eco}}$, which is the counterpart of GPP, is calculated as

$$\mathrm{R}_{\mathrm{eco}} = \sum_{v}^{\mathrm{N_{PFT}}} (\alpha_v T_{2\mathrm{m}} + \beta_v) \mathrm{veg}_{\mathrm{frac},v}, \qquad v \in \{\mathrm{ENF}, \mathrm{DBF}, \mathrm{MF}, \mathrm{SHB}, \mathrm{SAV}, \mathrm{CRO}, \mathrm{GRA}, \mathrm{OTH}\} \tag{7}$$

where α_v is the temperature sensitivity (μmol m^{-2} s^{-1} °C^{-1}), and β_v the base respiration rate (μmol m^{-2} s^{-1}). Both α_v and β_v are PFT-specific empirical parameters that were derived from FLUXNET data.

2.2.1 Optimization of VPRM parameters for the Alps

The ALPS parameters of VPRM were optimized against nineteen FLUXNET2015 sites to obtain PFT-specific values, fifteen sites located in the European Alps (44 to 50°N, 5 to 17°E), supplemented by four additional European sites in the region (Table D2 in Appendix D2) to account for underrepresented PFTs in cropland (CRO) and broadleaf forest (DBF).

Furthermore, there is little shrubland (SHB) and hardly savanna (SAV) in domain d03 (Fig. 2), neither any FLUXNET sites in, or close to, domain d01 (Fig. 1), therefore parameters for SHB and SAV were not optimized and the VPRM defaults were

https://doi.org/10.5194/egusphere-2026-939
Preprint. Discussion started: 8 May 2026

used. For each year at a site (hereafter referred to as a site-year), parameters were optimized separately for each of the 181 available site-years. Three different parameter settings per PFT were implemented into WRF-VPRM. "DF" corresponds to the default VPRM European parameters in WRF, "ALPS" represents the custom parameterization using all sites and all site-years with valid data. In addition, five sites located within domain d03 were optimized individually for the respective site and the year 2012, which defines a third parameter set, referred to as SITE. For SITE, optimum temperatures were optimized individually per location, making them specific to the altitude and weather in 2012 of the five FLUXNET sites and their respective PFT.

The optimization procedure follows Ranit et al. (2025), using GPP and R_{eco} as targets separately. Quality control of the training data followed the FLUXNET2015 flag convention, where only measured ($= 0$) and high-quality gap-filled ($= 1$) data are retained. Years with more than 20% missing values were excluded here. The applied products were based on the nighttime (NT) flux partitioning method, which estimates R_{eco} from nighttime NEE, and the variable friction velocity (u_*) threshold (VUT) approach, which accounts for site- and season-specific turbulence conditions in order to minimize low-turbulence biases in flux partitioning. The combination NT_VUT and optimizing GPP and R_{eco} individually, thus ensured robust separation across sites and years and that parameters are constrained by their respective dominant flux components, minimizing cross-correlation effects between GPP and R_{eco} during optimization (Ranit et al., 2025; Pastorello et al., 2020).

For parameter estimation, differential evolution (DE), a population-based genetic optimization algorithm from the Python SciPy library (Storn and Price, 1997; Gommers et al., 2024), was applied to minimize the differences between modeled and observed fluxes. Furthermore, the weighted NNSE was applied as defined in Appendix A. It incorporates a normalized random uncertainty weight $\sigma_{weight,t}$ that allocates higher weight to values with lower uncertainties, thereby making the parameter estimation more robust against noisy or unreliable FLUXNET eddy covariance measurements.

Meteorological input variables included T_{2m} and S↓. In contrast to many VPRM applications that rely on a PAR conversion (PAR = S↓/0.505), S↓ from FLUXNET was used directly here (PAR = S↓) to ensure consistency with the default WRF implementation, as mentioned in Sect. 2.2. The European DF parameters of WRF and the parameters calibrated for ALPS are listed in Table D3 and the site specific SITE parameters in Table D4.

There is no dedicated publication on the VPRM parameters that are currently implemented in WRF-VPRM. However, Glauch et al. (2025) highlight the methodological differences between the original VPRM and the updated pyVPRM framework: the default WRF-VPRM parameters were determined (similar to Gerbig (2024)) using a single-step fitting of both daytime and nighttime NEE data, while pyVPRM employs a two-step optimization, first fitting respiration parameters to nighttime fluxes and subsequently optimizing photosynthetic parameters using daytime data, similar to Ranit et al. (2025) and the approach presented here. Hence, the default WRF-VPRM parameters (DF) were calibrated using Europe-wide flux data and a single-step optimization that jointly fits daytime and nighttime NEE, which differs fundamentally from the two-step approach applied here for Alpine- (ALPS) and site-specific (SITE) parameters.

Simulations were performed with the three different VPRM parameter sets SITE, ALPS and DF, while CAMS served as an external dataset for comparison. To avoid mismatches due to topographic heterogeneity, model values were not taken directly at the site coordinates (see Fig. 2b). Instead, the closest representative grid-point was selected within a 30 km radius (in an approach similar to that proposed by Simonet et al. (2025)). Differences in model slope, aspect, elevation and PFT relative

https://doi.org/10.5194/egusphere-2026-939
Preprint. Discussion started: 8 May 2026

to the real site are minimized with a cost function. As the actual slope and aspect were not available, they are approximated by using the model values from the nearest grid-point of the 1 km grid to the actual site location. For example at IT-MBo, its validation grid-point contains a 90% fraction of grassland (GRA) and differs in elevation by 90 m from the tower site, while slope and aspect are nearly identical between the model grid-point and the site location. In contrast, CAMS values were linearly interpolated to the real FLUXNET locations, therefore comparability remains limited because CAMS height level differs. Additionally, CAMS employs a different biospheric model which performance varies regionally and in the seasonal cycle (Custódio et al., 2022).

2.2.2 Optimum temperature of plant functional types

Plants acclimate to prevailing temperatures by adjusting their physiological processes to optimize photosynthesis and respiration under local thermal conditions (Kattge and Knorr, 2007; Liu, 2020). Ecosystems within the European Alps are exposed to substantial local contrasts in altitude and ambient temperature. To partly account for this, a PFT-specific T_{opt} was determined for the Alps. $T_{2\mathrm{m}}$ and NEE data from nineteen FLUXNET sites and 181 site-years were used to derive representative T_{opt} values for VPRM optimization. Both variables were resampled to daily resolution to obtain mean daily temperature and NEE.

For each site-year, temperature values were grouped to bins of 1°C and NEE and $T_{2\mathrm{m}}$ were averaged accordingly. In a stepwise iteration first using a bell-shaped Gauss curve and second a quadratic polynomial was fitted to NEE as a function of temperature (Fig. E1). The quadratic polynomial accounts for situations in which the highest measured $T_{2\mathrm{m}}$ does not reach T_{opt}, such that T_{opt} lies outside the observed temperature range. The temperature at which the fit reaches its minimum is identified as T_{opt}. The site-year-specific T_{opt} is either determined as a "true" minimum from the Gaussian fit or otherwise approximated at or above the highest observed temperature for the polynomial fit in case no "true" minimum could be found. For each site-year, if at least 50% of "true" minima were available, their mean was used directly as T_{opt}. Otherwise, the mean of the extrapolated polynomial values, combined with available "true" minima, was applied. In particular for cropland (CRO), it was not possible to find an optimum temperature due to harvesting events, hence the default value is used.

2.3 Linear perturbation analysis of GPP differences

To assess the contribution of individual drivers to the differences in simulated GPP between model resolutions, a linear perturbation analysis was applied. This approach assumes that GPP responds approximately linearly to small changes in each driver, which is reasonable for incremental differences between resolutions. Linear perturbation analysis is based on Taylor series expansion similar to driver-sensitivity decompositions used in previous land-surface flux studies (e.g. Igarashi et al., 2015; Hu et al., 2023), but only for the linear first order term of the Taylor series. The method allows for separating the effects of multiple drivers while maintaining the spatial structure of the data. Regularization ensures numerical stability in cases where drivers are correlated or the system is ill-conditioned.

By applying this approach per grid-point and subsequently averaging over the domain, both spatial patterns and domain-mean contributions of each driver were obtained, enabling a detailed assessment of which environmental factors contribute most to the differences in GPP between model resolutions.

https://doi.org/10.5194/egusphere-2026-939
Preprint. Discussion started: 8 May 2026

Coarse-resolution data were interpolated to the 1 km grid prior to differencing, while $\mathrm{GPP}_{1\mathrm{km}}$ and GPP_{coarse} denote the fine (1 km) and coarse GPP fields, respectively. The difference is defined as

$$\Delta_{\mathrm{res}}\mathrm{GPP} = \mathrm{GPP}_{coarse} - \mathrm{GPP}_{1\mathrm{km}}. \tag{8}$$

Similarly, for each driver $x_i \in \{\lambda_v, T_{\mathrm{scale},v}, \mathrm{W}_{\mathrm{scale},v}, \mathrm{P}_{\mathrm{scale},v}, \mathrm{RAD}_v, \mathrm{EVI}_v\}$, the per grid-point difference in the driver is

$$\Delta_{\mathrm{res}} x_i = x_{i,\mathrm{coarse}} - x_{i,1\,\mathrm{km}}. \tag{9}$$

where Δ_{res} denotes the difference between coarse- and fine-resolution fields. Assuming that the change in GPP responds approximately linearly to the drivers, the following relation holds:

$$\Delta_{\mathrm{res}}\mathrm{GPP} \approx \sum_i \frac{\partial \mathrm{GPP}}{\partial x_i} \Delta_{\mathrm{res}} x_i + \varepsilon, \tag{10}$$

where $\frac{\partial \mathrm{GPP}}{\partial x_i}$ denotes the sensitivity of GPP for all PFT to the respective driver x_i. The residual term ε contains the nonlinear contributions of all drivers. A detailed derivation is demonstrated in Appendix B.

2.4 Changes to the WRF-VPRM code

2.4.1 Parallel computation of VPRM CO_2 fluxes

To systematically compare different VPRM parameterizations within one modeling framework, the WRF source code was extended to allow parallel computation of multiple VPRM parameter sets. In this setup, CO_2 fluxes and tracer fields for each parameter set were calculated simultaneously and written to separate diagnostic output streams. This avoided the need for repeated full model runs and guaranteed that all parameterizations were evaluated under identical meteorological and boundary conditions.

This enabled CO_2 fluxes from DF, ALPS, and SITE to be tracked independently throughout the simulation, while preserving computational efficiency and full consistency with WRF dynamics and physics. The implementation included three parameter sets, which are shown in the Appendix D: the default WRF-VPRM parameters (DF; Table D3), the Alpine-optimized (ALPS; Table D3), and the site-specific parameters (SITE; Table D4). For each of these parameter sets, additional fields for GPP, $\mathrm{R}_{\mathrm{eco}}$ and CO_2 were added in WRF, together with corresponding entries in the physics driver and output registry.

2.4.2 CORINE land-use representation and aggregation

High-resolution CORINE data were incorporated into the WRF-VPRM model to improve the representation of surface characteristics (de Bode et al., 2023). In WRF a dedicated 44-class look-up table for surface parameters, specifically designed for the CORINE data set, was implemented to avoid information loss relative to mappings onto existing schemes such as USGS. The look-up table extended the standard WRF land-use and vegetation parameter tables by providing key physical parameters-including albedo, available soil moisture, emissivity, roughness length (z_0), and thermal inertia, for all 44 CORINE classes. Although the table contained 44 entries, the initial parameter specification effectively reduced the number of distinct

https://doi.org/10.5194/egusphere-2026-939
Preprint. Discussion started: 8 May 2026

land-surface types to 28 due to clustering within artificial surfaces, consistent with de Bode et al. (2023). In addition, the 44 CORINE classes were remapped (Table D1) to the eight VPRM plant functional types (PFTs) used for biosphere-atmosphere exchange calculations in VPRM as described in Sect. 2.1.

2.4.3 Analytical temperature derivatives of biospheric CO_2 fluxes

To quantify the temperature sensitivity of biospheric CO_2 fluxes in WRF-VPRM, the partial derivatives of GPP and R_{eco} with respect to T_{2m} were computed analytically within the model. The derivatives are calculated online before fluxes from different PFT are aggregated within a grid cell, ensuring that the PFT-specific temperature response is preserved. An illustrative example is shown in Fig. 3a, where P_{scale}, W_{scale}, RAD and EVI are held constant. The derivative of GPP (Eq. (2)) with respect to temperature for the sum of the PFT fractions is

$$\frac{\partial \mathrm{GPP}}{\partial T_{2m}} = \sum_{v}^{N_{PFT}} \lambda_v \frac{\partial T_{scale,v}}{\partial T_{2m}} P_{scale,v} W_{scale,v} \mathrm{RAD}_v \mathrm{EVI}_v \mathrm{veg}_{frac,v}, \tag{11}$$

where $\mathrm{veg}_{frac,v}$ is the vegetation fraction and v indicates the individual PFT.

For ecosystem respiration, the temperature derivative of R_{eco} (Eq. (7)) is

$$\frac{\partial \mathrm{R_{eco}}}{\partial T_{2m}} = \sum_{v}^{N_{PFT}} \alpha_v \mathrm{veg}_{frac,v}, \tag{12}$$

which only depends on the PFT dependent temperature sensitivity α_v. Due to differentiation the constant base respiration rate β_v is eliminated and $R_{eco,v}$ reduces to one. The full differentiation is shown in Appendix C.

At the PFT dependent optimum temperatures the sign of $\frac{\partial \mathrm{GPP}}{\partial T_{2m}}$ changes (Fig. 3b), it is positive below $T_{opt,v}$ and negative above, consistent with a maximum in GPP, simultaneously its magnitude and shape is PFT-dependent through the parameters λ_v, $\mathrm{PAR}_{0,v}$ and $T_{opt,v}$. Values below 5°C are not included in the analysis, as the derivative becomes unrealistically high, which remains a limitation of this approach in low temperature environments. The derivative $\frac{\partial \mathrm{R_{eco}}}{\partial T_{2m}}$ is a constant line dependent on the PFT-specific parameter α_v.

https://doi.org/10.5194/egusphere-2026-939
Preprint. Discussion started: 8 May 2026

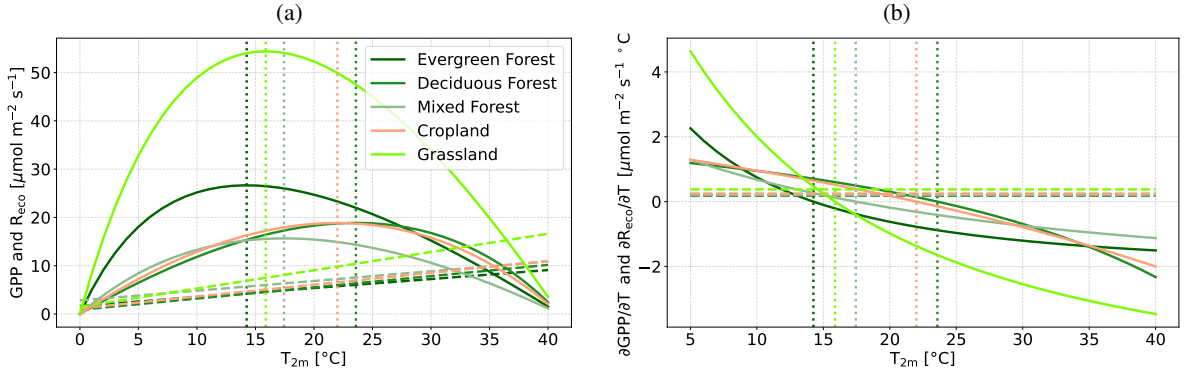

Figure 3. VPRM flux response and temperature sensitivity of plant functional type (PFT). Panel (a) displays gross primary production (GPP, solid lines) and ecosystem respiration (R_{eco}, dashed lines) derived from optimized VPRM parameters as a function of 2 m air temperature (T_{2m}). Panel (b) shows the temperature sensitivity of GPP ($\frac{\partial GPP}{\partial T_{2m}}$, solid lines) and R_{eco} ($\frac{\partial R_{eco}}{\partial T_{2m}}$, dashed lines). The optimum temperature (T_{opt}) for PFT is indicated by dotted vertical lines in both panels. Other terms of Eq. (2), phenology (P_{scale} = 0.5), water stress (W_{scale} = 0.5), irradiance (RAD = 500 μmol m^{-2} s^{-1}) and the enhanced vegetation index (EVI = 1), are held constant.

3 Results

3.1 Validation against FLUXNET sites

At the FLUXNET grassland site Monte Bondone (IT-MBo, 1550 m AMSL, Italy), modeled CO_2 fluxes of 24 days and from different VPRM parameter sets were evaluated against observations (Fig. 4). IT-MBo was selected because it exhibited the best overall model-data agreement. Analogous results are shown for the alpine sites Neustift (AT-Neu, GRA), Renon (IT-Ren, ENF), Davos (CH-Dav, ENF), and Lavarone (IT-Lav, ENF) in Appendix E (Figs. E2–E5). An overview of SITE, ALPS, and DF performance is provided in Appendix D. Table D5 lists site-level mean FLUXNET observations, mean bias (MB), and mean absolute error (MAE) for the 24 sampled days. The limited effective sample size increases sensitivity to the selected hours and prevailing weather regimes, introducing substantial sampling uncertainty. Under these conditions, MAE and MB provide the most robust and interpretable summaries of model performance. RMSE and R^2 are reported in Table D7 in Appendix D primarily for completeness. Note that the SITE parameter set for sites located in domain d03, was created exclusively for this validation, for 2 of 6 GRA sites from domain d01 and accordingly 3 of 5 ENF sites (Appendix D, Table D2).

For IT-MBo (Fig. 4), the WRF T_{2m} exhibits a cold bias, while among the parameter sets, SITE achieves the smallest systematic errors in both GPP and R_{eco}, while ALPS substantially overestimates GPP and DF strongly underestimates both components. Although DF produces a small mean NEE bias, its MAE is nine times larger than its MB, confirming that apparent agreement results from compensating errors in GPP and R_{eco} rather than accurate flux representation. Detailed MB and MAE values are listed in Appendix D (Table D5).

The coarse CAMS grid precludes a quantitative site-scale evaluation, as with DF, its apparent NEE agreement reflects compensating errors in GPP and R_{eco} rather than realistic flux estimates.

https://doi.org/10.5194/egusphere-2026-939
Preprint. Discussion started: 8 May 2026

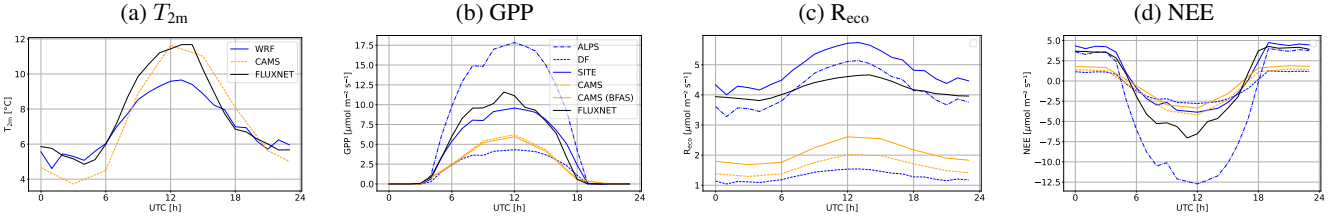

Figure 4. Validation of mean diurnal cycles at the FLUXNET site Monte Bondone (IT-MBo). Hourly averages are shown for all simulations, over 12 clear-sky and 12 cloudy/rainy days in 2012. In (a) for 2 m air temperature (T_{2m}), in (b) gross primary production (GPP), in (c) ecosystem respiration (R_{eco}), and in (d) net ecosystem exchange (NEE). Observed FLUXNET (solid black) values are compared to three VPRM parameter sets SITE (solid blue), ALPS (dash-dotted blue), and DF (dashed blue). CAMS data is shown with (solid orange) and without (dashed orange) the Biogenic Flux Adjustment Scheme (BFAS) correction.

The multi-site mean behavior (Table D5) supports the findings at IT-MBo: all parameter sets show a persistent cold bias in T_{2m}, SITE exhibits the smallest systematic errors in both component fluxes, while ALPS overestimates uptake and DF strongly underestimates both GPP and R_{eco}. Overall, SITE provides the most consistent component-flux representation, while DF's apparently favorable NEE bias arises from cancellation of large but opposing component-flux errors.

To assess whether the 24 modeled days provide a representative sampling of the annual cycle, Table D6 in Appendix D compares FLUXNET measurements at all ALPS locations (which include SITE) restricted to the selected clear-sky and cloudy/rainy days with the corresponding full-year averages for 2012. Site-level temperatures during the sampling period are substantially higher at all sites (2.75 °C) than the annual mean, resulting in a stronger apparent carbon sink, with NEE approximately 20% lower (higher uptake of CO_2) than for the full-year observations for ALPS.

Consequently, while the relative ranking of the SITE, ALPS, and DF parameter sets provides useful guidance, it should be regarded as indicative given the limited sample size and the inherent difficulty of tuning ecosystem models in heterogeneous mountainous terrain. A more definitive evaluation would require continuous multi-annual WRF-VPRM simulations and denser observational coverage. Given that SITE was optimized specifically for these five locations, its superior performance is expected. However, only ALPS and DF are applicable across the full domain, SITE therefore serves primarily as a benchmark. Hence, the domain-wide results from ALPS and DF presented in the following sections must be interpreted in light of their demonstrated systematic biases.

3.2 Topographic impact on domain-averaged CO_2 fluxes

3.2.1 Clear sky conditions

To illustrate the overall impact of model resolution and parameter choice (ALPS vs. DF), simulated CO_2 fluxes are averaged over mountainous grid-points of domain d03 (see Fig. 1b). The analyzed variables include T_{2m}, S↓, GPP, R_{eco} and NEE. All variables are averaged per hour of the day over 12 clear-sky days distributed across 2012, as shown in Fig. 5(a)–(e) (individual daily timeseries are in Appendix E, Fig. E6–E10). Seasonally varying but daily constant vegetation indices (LSWI and EVI,

https://doi.org/10.5194/egusphere-2026-939
Preprint. Discussion started: 8 May 2026

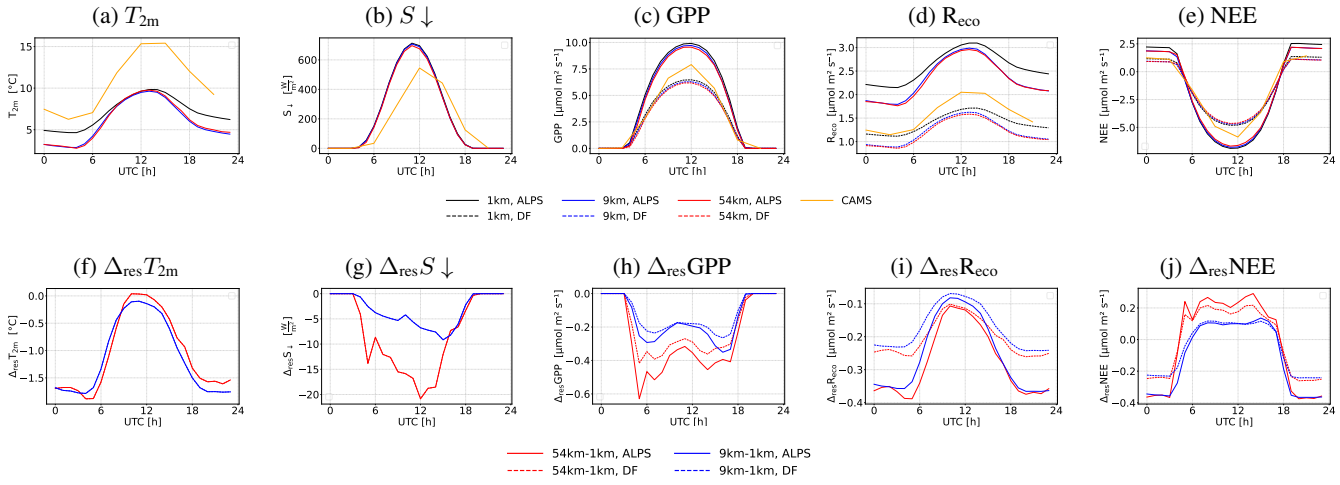

Figure 5. Domain-averaged time series for 12 days under clear-sky conditions throughout 2012. Panels (a)–(e) show the course of the day of 2 m air temperature (T_{2m}), shortwave downward radiation ($S\downarrow$), gross primary production (GPP), ecosystem respiraiton (R_{eco}), and net ecosystem exchange (NEE), simulated at 1 km (black), 9 km (blue), and 54 km (red) grid spacings, using VPRM with ALPS (solid lines) and DF (dashed lines) parameters, alongside CAMS averages (yellow). Panels (f)–(j) show the corresponding differences of WRF-VPRM: 9 km–1 km (blue) and 54 km–1 km (red).

updated in 8-day intervals) also influence the simulated CO_2 fluxes (they are not shown here but investigated in Sect. 3.3.2). Note that the SITE parameter sets can not be applied over the full domains, as they were exclusively tuned for evaluation of individual sites and cannot represent spatial fluxes.

To compare different grid spacings, coarser domain output is interpolated to the 1 km grid using the nearest-neighbor method. This approach preserves absolute values and avoids artificial smoothing artifacts that may arise from bilinear or higher-order interpolation. Differences between coarse and fine resolutions shown in Fig. 5(f)–(j) are defined as

$$\Delta_{res}x_i = x_{i,\text{coarse}} - x_{i,1\,\text{km}}, \qquad x_i \in \{T_{2\,\text{m}}, \text{S}\downarrow, \text{GPP}, \text{R}_{\text{eco}}, \text{NEE}\}. \tag{13}$$

In VPRM, both GPP and R_{eco} respond strongly to T_{2m} and S$\downarrow$. Warmer T_{2m} increases respiration exponentially, whereas the increase or decrease of GPP depends on T_{opt}, while higher S$\downarrow$ directly enhances GPP. Thus, differences between coarse and high-resolution in temperature ($\Delta_{res}T_{2m}$) and radiation (Δ_{res}S$\downarrow$) modify NEE by shifting GPP and R_{eco}. On clear-sky days, $\Delta_{res}T_{2m}$ is mostly negative at 9 and 54 km, indicating warmer temperatures in the 1 km run (Fig. 5(a)). If T_{2m} is below (above) T_{opt} a negative (positive) $\Delta_{res}T_{2m}$ results in higher GPP at 1 km. For radiation this is even more pronounced, i.e. at 9 km and 54 km Δ_{res}S$\downarrow$ is negative throughout the day indicating higher GPP at 1 km. However, the net effect is modest, for both 9 and 54 km, and Δ_{res}NEE is slightly positive during daytime as $\Delta_{res}T_{2m}$ and Δ_{res}S$\downarrow$ are as well close to zero. The main part of Δ_{res}NEE during clear-sky days is caused by negative $\Delta_{res}T_{2m}$ at night which results in higher R_{eco} at the 1 km grid spacing (Fig. 5(j)).

https://doi.org/10.5194/egusphere-2026-939
Preprint. Discussion started: 8 May 2026

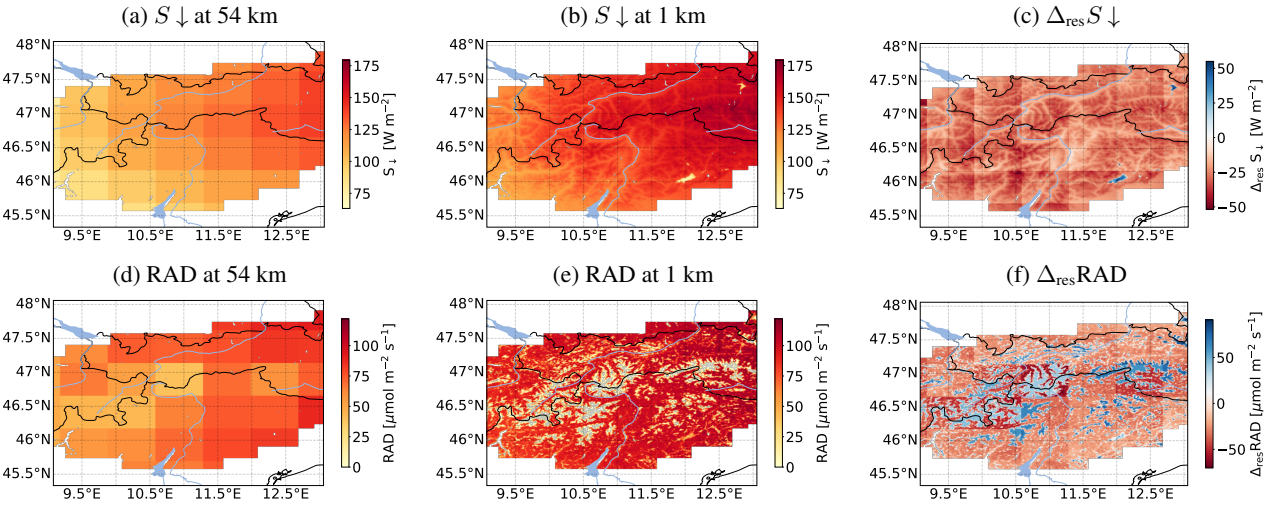

Figure 6. Spatial analysis of radiation components on 27 July 2012 at 05:00 UTC over WRF domain d03. Panels (a)–(b) show the shortwave downward radiation ($S\downarrow$) at 54 km and 1 km grid spacing, respectively. Panels (d)–(e) show the calculated irradiance contribution (RAD) of all PFT at 54 km and 1 km grid spacing. The respective differences are shown for $\Delta_{res}S\downarrow$ in (c) and for Δ_{res}RAD in (f).

As 3-hourly CAMS data originate from a different atmospheric and biological model, its values are shown in Fig. 5(a)-(e) for comparison, but are not used for evaluation. CAMS exhibits systematically higher T_{2m} and lower S$\downarrow$ than WRF. NEE from CAMS is close to the DF simulations (Fig. 5(e)), but as visible in Fig. E10 the similar average NEE fluxes are coincidental, resulting from CAMS being higher than all WRF runs in winter and lower in summer.

Figure 6 shows the spatial distribution of S$\downarrow$ and RAD at 54 km and 1 km grid spacing for a morning hour when differences are most pronounced. At 54 km, smoothed topography suppresses slope-aspect effects, whereas the 1 km grid resolves locally enhanced radiation on sun-facing slopes, rendering Δ_{res}S$\downarrow$ systematically negative. The resulting Δ_{res}RAD shows strong spatial contrasts reflecting differences in vegetation cover superimposed on Δ_{res}S$\downarrow$, which compensate across the domain to yield only small net differences in the domain average. Because these area maps are dominated by local extremes rather than meaningful spatial patterns similar maps are not shown for other variables that depend on the vegetation fraction.

The quantitative effects of parameter optimization and grid spacing are summarized in Table 1. Across all resolutions, the DF parameter set yields systematically lower values of GPP and R_{eco}. Under clear-sky conditions at 1 km, DF reaches 64% and 54% of ALPS GPP and R_{eco}, respectively, and 80% for NEE. This difference arises from the tuning of ALPS parameters (λ, PAR_0, α, and β) to alpine FLUXNET sites, as well as from the lower T_{opt} values in ALPS, which enhances NEE under the cooler conditions characteristic of higher elevations.

Results under clear-sky conditions indicate that parameter optimization (ALPS vs. DF) exerts a stronger influence on simulated NEE than changes in grid spacing. Resolution-dependent differences relative to the 1 km grid ($\frac{|\Delta_{res}NEE|}{|NEE_{1km}|}$) amount to 7% (ALPS) and 4% (DF) at 9 km, and 2% (ALPS) and 1% (DF) at 54 km. These differences occur dominantly at night, while at 54 km the effect of coarser radiation fields partly compensates them, thereby reducing Δ_{res}NEE.

https://doi.org/10.5194/egusphere-2026-939
Preprint. Discussion started: 8 May 2026

Table 1. Domain-averaged values from 2012 of 12 clear-sky days (upper section) and 12 cloudy/rainy days (lower section) for each variable $x_i \in \{T_{2\mathrm{m}}, \mathrm{S}\downarrow, \mathrm{GPP}, \mathrm{R_{eco}}, \mathrm{NEE}\}$, grid spacing, and simulation type ($\mathrm{STD_{TOPO}} > 200$; VPRM with optimized ALPS and reference DF parameters, and CAMS). For the 1 km column, values in square brackets indicate DF values relative to ALPS, i.e. $\frac{|x_{i,\,1\mathrm{km,\,DF}}|}{|x_{i,\,1\mathrm{km,\,ALPS}}|}$ in percent. For the remaining columns at coarser resolutions, values in parentheses denote absolute differences to the 1 km ALPS or DF simulation ($\Delta_{\mathrm{res}} x_i$), respectively. Relative differences in square brackets are given as positive percentages based on absolute values, i.e. $\frac{|\Delta_{\mathrm{res}} x_i|}{|x_{i,\,1\mathrm{km}}|}$. Bold values highlight the largest absolute and relative differences in NEE. The last row shows approximate yearly NEE averages from both clear-sky and cloudy/rainy results, values in brackets are calculated with the same logic.

Clear Sky	1 km		9 km		54 km		CAMS
	ALPS	DF	ALPS	DF	ALPS	DF	
$T_{2\mathrm{m}}$ [°C]	7.09		5.96 (-1.13 [16%])		6.03 (-1.06 [15%])		10.58 (3.54 [50%])
S↓ [W m^{-2}]	226.88		223.60 (-3.28 [1%])		219.08 (-7.80 [3%])		180.09 (-46.82 [21%])
GPP [μmol m^{-2} s^{-1}]	4.27	2.74 [64%]	4.12 (-0.15 [3%])	2.62 (-0.12 [4%])	4.01 (-0.25 [6%])	2.54 (-0.20 [7%])	2.99 (-1.29 [30%])
$\mathrm{R_{eco}}$ [μmol m^{-2} s^{-1}]	2.59	1.39 [54%]	2.34 (-0.26 [10%])	1.22 (-0.17 [13%])	2.31 (-0.28 [11%])	1.19 (-0.20 [15%])	1.57 (-1.02 [39%])
NEE [μmol m^{-2} s^{-1}]	-1.67	-1.34 [80%]	-1.78 **(-0.11 [7%])**	-1.40 **(-0.05 [4%])**	-1.70 **(-0.03 [2%])**	-1.35 **(-0.01 [1%])**	-1.42 (0.27 [16%])
Clouds and rain	1 km		9 km		54 km		CAMS
	ALPS	DF	ALPS	DF	ALPS	DF	
$T_{2\mathrm{m}}$ [°C]	2.32		2.08 (-0.24 [10%])		2.52 (0.21 [9%])		7.52 (5.10 [220%])
S↓ [W m^{-2}]	148.45		143.48 (-4.97 [3%])		128.72 (-19.73 [13%])		110.82 (-37.90 [26%])
GPP [μmol m^{-2} s^{-1}]	2.45	1.59 [65%]	2.26 (-0.19 [8%])	1.46 (-0.13 [8%])	1.91 (-0.53 [22%])	1.21 (-0.38 [24%])	1.94 (-0.54 [21%])
$\mathrm{R_{eco}}$ [μmol m^{-2} s^{-1}]	1.85	0.95 [52%]	1.73 (-0.12 [6%])	0.88 (-0.08 [8%])	1.72 (-0.12 [7%])	0.85 (-0.11 [11%])	1.26 (-0.60 [32%])
NEE [μmol m^{-2} s^{-1}]	-0.60	-0.64 [107%]	-0.53 **(0.07 [12%])**	-0.58 **(0.05 [8%])**	-0.19 **(0.41 [68%])**	-0.36 **(0.27 [43%])**	-0.67 (-0.07 [12%])
Approx. yearly NEE	1 km		9 km		54 km		CAMS
NEE [μmol m^{-2} s^{-1}]	-1.14	-0.99 [87%]	-1.16 **(0.02 [2%])**	-0.99 **(0 [0%])**	-0.95 **(0.19 [17%])**	-0.86 **(0.13 [13%])**	-1.05 (0.10 [8%])

CAMS CO_2 fluxes strongly deviate from the WRF-VPRM simulations, particularly under clear-sky conditions. There, temperature is 50% higher while radiation is 21% lower than WRF at 1 km. Consequently, CAMS yields GPP values 30% lower and $\mathrm{R_{eco}}$ 39% lower than the 1 km ALPS simulation, resulting in markedly reduced NEE of 16%.

3.2.2 Cloudy and rainy conditions

On cloudy and rainy days, DF reproduces 65% of ALPS GPP and 52% of $\mathrm{R_{eco}}$ at 1 km, consistent with clear-sky behavior, as summarized in Table 1. However, DF reaches 107% of ALPS NEE under cloudy/rainy conditions, compared to 80% under clear-sky conditions. This apparent improvement again reflects offsetting errors between photosynthesis and respiration rather than accurate flux representation.

Under cloudy/rainy conditions, temperature and radiation differences show reduced amplitude compared to clear-sky, with $\Delta_{\mathrm{res}} T_{2\mathrm{m}}$ at 54 km almost consistently positive and $\Delta_{\mathrm{res}} \mathrm{S}\downarrow$ predominantly negative (individual daily timeseries in Appendix E, Figs. E11–E15). At 9 km, NEE differences remain comparable in absolute magnitude to clear-sky days (Table 1). At 54 km, however, the compensating radiation effects observed under clear-sky conditions become one-sided, with predominantly neg-

https://doi.org/10.5194/egusphere-2026-939
Preprint. Discussion started: 8 May 2026

ative $\Delta_{res}S\downarrow$ driving substantially larger NEE differences, reaching 68% for ALPS and 43% for DF, compared to only 2% and 1% under clear-sky conditions.

Under cloudy/rainy conditions, CAMS NEE aligns more closely with the ALPS simulations than under clear-sky, again reflecting compensating effects between its higher T_{2m} and lower S↓.

The approximate yearly NEE reported in the last row of Table 1 is obtained as a first-order estimate by averaging the 24 analysed days (12 clear-sky and 12 cloudy/rainy days) and should therefore be regarded as indicative rather than representative of a true annual mean. Relative to ALPS at 1 km, the approximate yearly NEE differs by only about 2% between 1 km and 9 km for ALPS and by 0% for DF. On the other hand, the choice of parameter sets at 9 km introduces a difference such that NEE(DF_{9km}) amounts to 85% of NEE($ALPS_{9km}$), thus again indicating that parameter tuning has a larger impact than resolution at this intermediate spatial scale. In contrast, the transition from 1 km to 54 km results in substantially larger deviations, reaching 17% for ALPS, which clearly exceeds the effect of parameter choice at 54 km (8%). For DF, the change from 1 km to 54 km amounts to 13% and is therefore slightly larger than the parameter-choice effect (8%).

While CAMS employs a distinct biosphere model with a different seasonal cycle and is optimized against meteorological drivers that differ from WRF-VPRM, specifically higher temperatures and lower radiation, its top-down constraint for the annual carbon budget makes the comparison of CAMS yearly averages a suitable basis for validating WRF-VPRM. The approximate yearly NEE of CAMS (Table 1) provides values that are in between ALPS and DF of WRF-VPRM, indicating that all results are within a realistic range for the yearly carbon budget (Custódio et al., 2022).

Overall, these results indicate that at coarse resolution the loss of spatial detail can dominate the uncertainty in yearly NEE, whereas at finer resolutions, differences between parameterizations become relatively more important than the resolution change itself.

3.3 Attribution of NEE differences to VPRM equation components

3.3.1 Temperature contributions to biospheric flux differences

When comparing modeled and observed temperatures, it is a common practice to interpolate model temperature to observation height using vertical temperature gradients (e.g., lapse-rate correction, linear or spline interpolation). Based on such corrections it is theoretically possible to approximate the temperature contribution to subgrid-scale fluxes of GPP and R_{eco}, of a climate simulation with O(100 km) grid spacing, by estimating the temperature differences based on a high-resolution topography O(1 km). A first step towards subgrid-scale parameterization is presented by Reif et al. (2024), who quantified the dependence of ecosystem CO_2 fluxes on temperature and VPD in an idealized valley compared to a flat reference simulation, applying a regression analysis (their Sect. 3.3). The approach aimed at capturing the distinct flux responses to temperature differences relative to the height-consistent temperature.

Here, as a next step, the analytical derivatives of GPP and R_{eco} with respect to temperature are computed for the model results as defined in Eq. (11) and (12), depicted for exemplary values in Fig. 3. By multiplying the difference of model temperatures at two grid spacings $\Delta_{res}T_{2m}$, under the assumption that temperature changes are on average small, the temperature-induced

https://doi.org/10.5194/egusphere-2026-939
Preprint. Discussion started: 8 May 2026

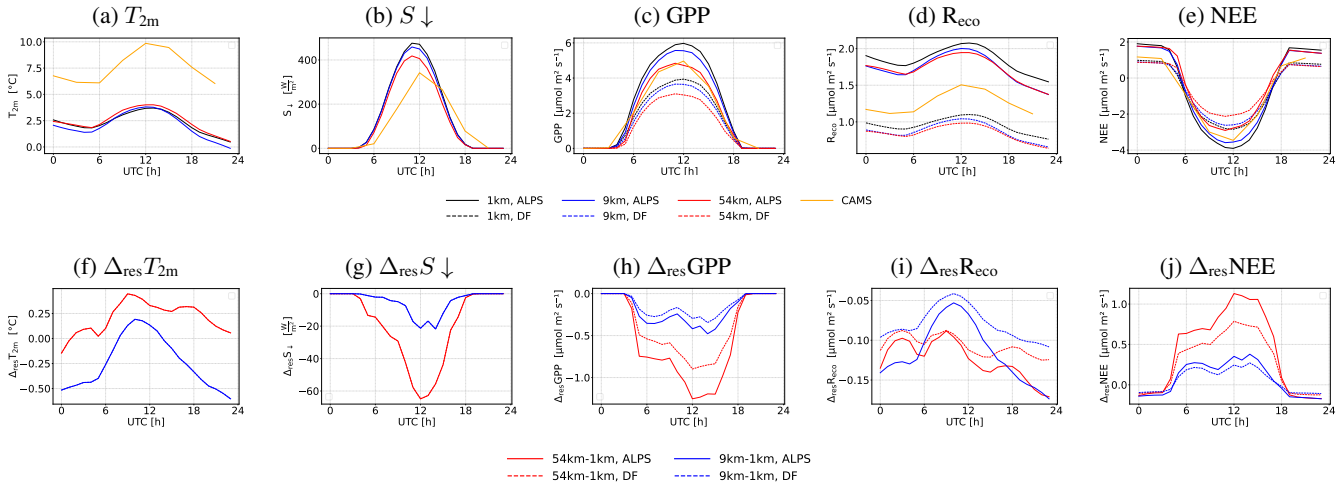

Figure 7. Domain-averaged time series for 12 days under cloudy/rainy conditions throughout 2012. Panels (a)–(e) show the course of the day of 2 m air temperature (T_{2m}), shortwave downward radiation ($S\downarrow$), gross primary production (GPP), ecosystem respiraiton (R_{eco}), and net ecosystem exchange (NEE), simulated at 1 km (black), 9 km (blue), and 54 km (red) grid spacing, using VPRM with ALPS (solid lines) and DF (dashed lines) parameters, alongside CAMS averages (yellow). Panels (f)–(j) show the corresponding differences Δ_{res} of WRF-VPRM: 9 km–1 km (blue) and 54 km–1 km (red).

difference can be calculated as

$$\Delta_{\partial T}\, x_i = \Delta_{\text{res}} T_{2\text{m}}\, \frac{\partial x_{i,1\text{km}}}{\partial T_{2\text{m, 1km}}} \qquad x_i \in \{\text{GPP}, \text{R}_{\text{eco}}\}, \tag{14}$$

where $\Delta_{\partial T}$ indicates that the temperature difference between grid spacings is approximated from $\Delta_{\text{res}}T_{2\text{m}}$ and the respective derivative.

Figure 8(a) illustrates the spatial heterogeneity of $\Delta_{\text{res}}T_{2\text{m}}$ between 54 and 1 km grid spacing on 27 July 2012 at 12:00 UTC. The temperature sensitivity $\frac{\partial \text{GPP}_{1\text{km}}}{\partial T_{2\text{m, 1km}}}$ (Fig. 8(b)) reveals strong negative spatial gradients, in lowland areas where $T_{2\text{m, 1km}}$ is above T_{opt} and values around zero at higher elevations where the temperature is close to T_{opt}. Multiplying this sensitivity with the actual temperature differences between coarse and fine resolutions yields the GPP changes due to temperature, i.e. $\Delta_{\partial T}$GPP (Fig. 8(c)). The example of 27 July 2012 at 12:00 UTC shows a rather extreme case, where it is relatively warm in the mountains and hot in the valleys. It highlights regions and weather conditions where temperature differences strongly alter the high-resolution CO_2 fluxes. Temperature mismatches translate into systematic biases in simulated GPP, while the effect is strongly modulated by the spatial distribution of vegetation productivity.

Figure 9 shows the total, domain and time averaged flux differences due to resolution and their contributions due to temperature alone, for all 24 days of simulations, at 9 and 54 km for ALPS and DF. Results from both weather conditions are merged because the temperature contributions retain the same sign. In Fig. 9(a) hourly averages of Δ_{res}GPP from all simulations are compared to the temperature contribution $\Delta_{\partial T}$GPP. The calculated temperature contributions $\Delta_{\partial T}$ indicate that a substantial

https://doi.org/10.5194/egusphere-2026-939
Preprint. Discussion started: 8 May 2026

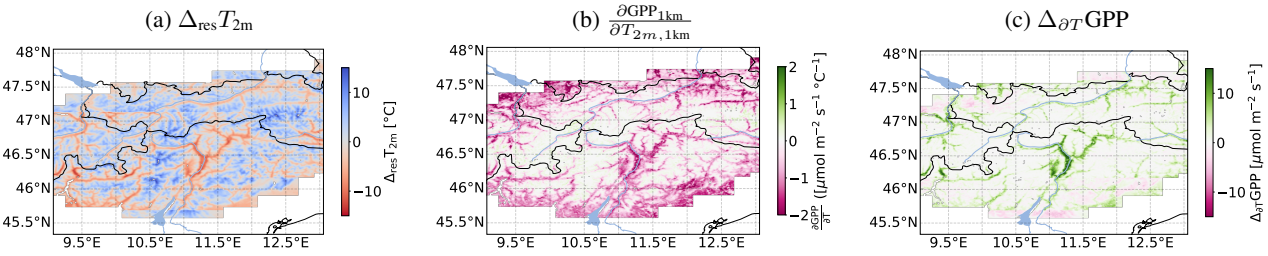

Figure 8. Spatial analysis of temperature contributions on 27 July 2012 at 12:00 UTC over WRF domain d03. Panel (a): temperature difference ($\Delta_{\text{res}}T_{2\text{m}}$) between the 54 km and 1 km grid spacing ($\Delta_{\text{res}}T_{2\text{m}} = T_{2m,54\text{km}} - T_{2m,1\text{km}}$). Panel (b): temperature sensitivity of GPP at 1 km grid spacing ($\frac{\partial \text{GPP}_{1\text{km}}}{\partial T_{2m,1\text{km}}}$). Panel (c): approximated GPP change due to the temperature difference ($\Delta_{\partial T}$GPP).

part of Δ_{res}GPP at both 54 and 9 km originates from temperature effects, which are strongest in the morning and weaken thereafter. For DF, the contributions are consistently shifted toward lower absolute values compared to ALPS. At 54 km, Δ_{res}GPP for both parameter sets is predominantly governed by radiation differences, as further analyzed in Sect. 3.3.2. For R_{eco} in Fig. 9(b), the amplitude of the temperature contribution is much smaller than for GPP but the daily cycles of $\Delta_{\text{res}}R_{\text{eco}}$ and $\Delta_{\partial T}R_{\text{eco}}$ are very similar, hence the temperature contribution explains the major part of $\Delta_{\text{res}}R_{\text{eco}}$.

Temperature explains approximately 35–42% of Δ_{res}GPP across resolutions and parameter sets, with the largest contributions during morning hours when both temperature and radiation gradients are strongest (percentage results are not shown in Fig. 9). In contrast, R_{eco}, which depends linearly on temperature, is predominantly thermally controlled: temperature explains 71–85% of $\Delta_{\text{res}}R_{\text{eco}}$ across all configurations, confirming that respiration is the component most directly correctable via temperature downscaling.

https://doi.org/10.5194/egusphere-2026-939
Preprint. Discussion started: 8 May 2026

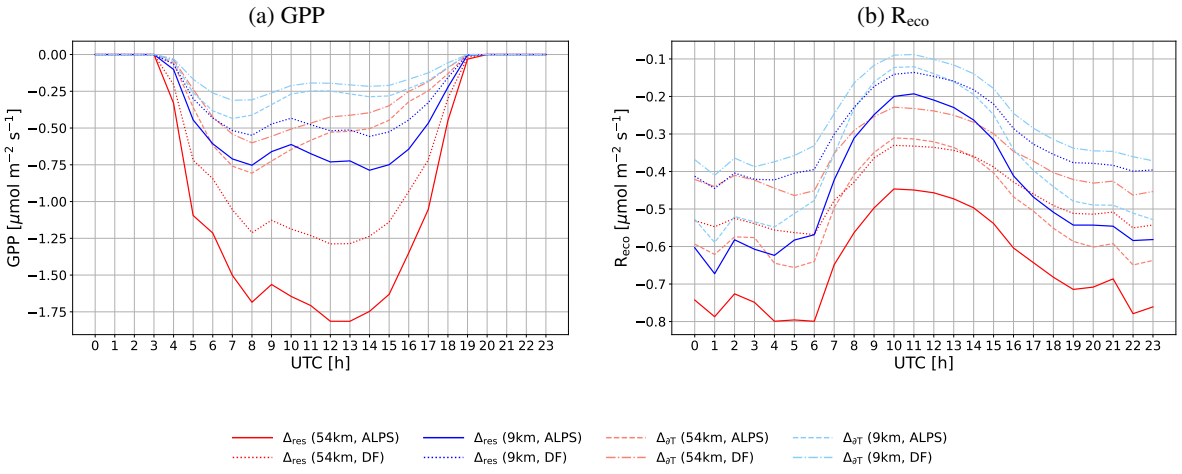

Figure 9. Comparison of the total, domain averaged (d03) flux differences (Δ_{res}) and temperature contributions ($\Delta_{\partial T}$) for 54 km and 9 km with respect to 1 km. Hourly domain means over d03 are shown for 2012 including both clear-sky and cloudy/rainy days. Panel (a) compares the total grid spacing difference Δ_{res}GPP for ALPS (solid lines) and DF (dotted lines) at 54 km (red) and 9 km (blue) with the contribution estimated from temperature sensitivity, $\Delta_{\partial T}$GPP (dashed and dash-dotted lines, respectively) at 54 km (orange) and 9 km (lightblue). Panel (b) shows the analogous comparison for R$_{\text{eco}}$.

3.3.2 Linear perturbation analysis of all VPRM components

Linear perturbation analysis decomposes the resolution-driven difference in GPP (Δ_{res}GPP) into domain-mean contributions

$$\overline{Y_{x_i}} = \overline{\Delta_{\text{res}} x_i \frac{\partial \text{GPP}}{\partial x_i}} \qquad x_i \in \{\lambda, T_{\text{scale}}, \text{W}_{\text{scale}}, \text{P}_{\text{scale}}, \text{RAD}, \text{EVI}\}, \tag{15}$$

for each environmental driver, which combines the driver anomaly and its sensitivity, so that $\overline{Y_{x_i}}$ reflects the absolute mean contribution of driver x_i to the resolution-dependent GPP difference.

Hourly averages in Fig. 10 show that $\overline{Y_{\text{RAD}}}$ dominates during morning and evening transition hours, with magnitudes up to -1 μmol m^{-2} s^{-1}. $\overline{Y_{\text{T}_{\text{scale}}}}$ contributes consistently throughout daytime with values up to -0.6 μmol m^{-2} s^{-1} (Fig. 10(a,c)), confirming its role as an important driver. In contrast to the input variables $\Delta_{\text{res}}T_{2\text{m}}$ and Δ_{res}S$\downarrow$ (Figs. 5 and 7), $\overline{Y_{T_{\text{scale}}}}$ and $\overline{Y_{\text{RAD}}}$ (Fig. 10) contribute directly to the final Δ_{res}GPP. The effects of $\overline{Y_{\lambda}}$ and the satellite-derived variables ($\overline{Y_{\text{W}_{\text{scale}}}}$, $\overline{Y_{\text{P}_{\text{scale}}}}$, $\overline{Y_{\text{EVI}}}$) primarily shift the baseline rather than to drive day-to-day variability. Satellite-derived variables employed here are updated every eight days, and the signs of their contributions remain constant throughout the year. The magnitude of these contributions is resolution dependent and reflects structural contrasts between model configurations. Residuals on clear-sky days are large at 54 km grid spacing, indicating that the nonlinear response cannot be captured. The shape of Δ_{res}S$\downarrow$ in Fig. 5(g) further suggests that it is the radiation pattern that contributes most to the residual. In contrast, the residuals in the other cases are small, implying that the linear decomposition adequately reproduces the main structure of the GPP differences.

https://doi.org/10.5194/egusphere-2026-939
Preprint. Discussion started: 8 May 2026

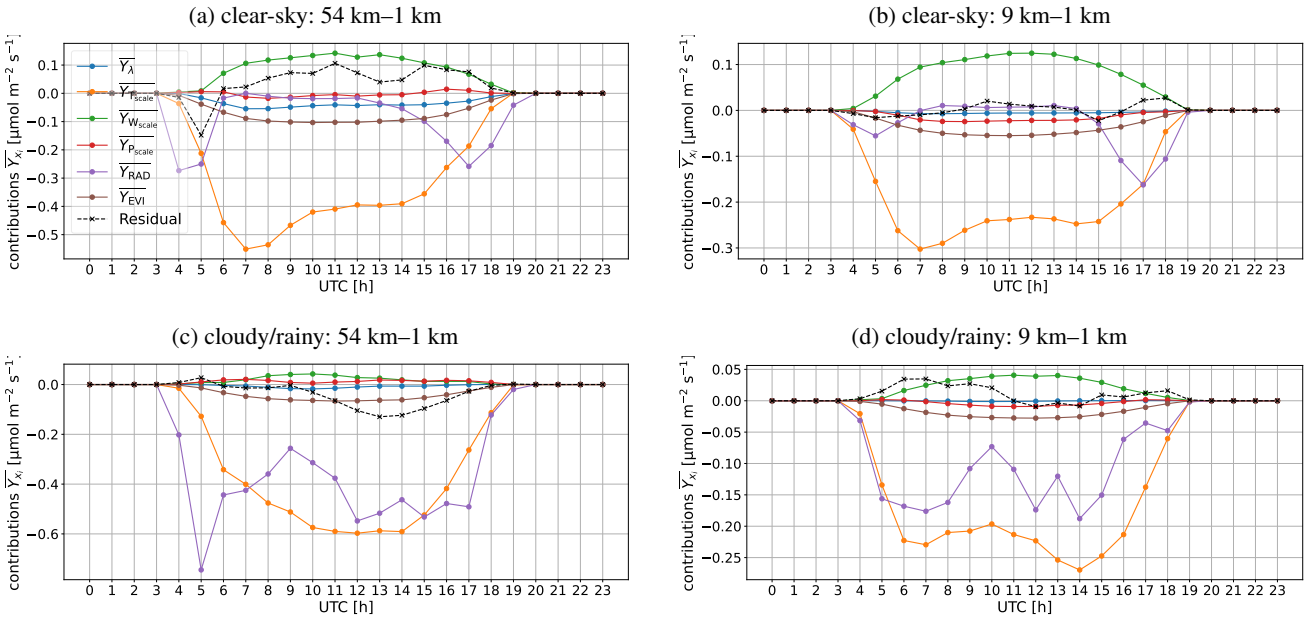

Figure 10. Linear perturbation analysis decomposing Δ_{res}GPP drivers for ALPS parameters average in 2012 over 12 days under clear sky and cloudy/rainy conditions, respectively. The figure shows the domain-averaged daily cycles $\overline{Y_{x_i}}$ of individual drivers $\Delta_{res}x_i$ to the total GPP difference Δ_{res}GPP between coarse and fine grid spacing (54 km and 9 km, relative to 1 km). Panels (a)–(b) show mean contributions under clear-sky conditions, and panels (c)–(d) show contributions under cloudy/rainy conditions. Negative contributions imply that the respective driver reduces Δ_{res}GPP, indicating higher uptake in the 1 km domain.

The perturbation analysis reveals that resolution-driven flux differences are systematic, with radiation ($\overline{Y_{\mathrm{RAD}}}$) and temperature contributions ($\overline{Y_{T_{\mathrm{scale}}}}$) dominating the signal at 54 km during mornings and evenings under clear-sky conditions, while they are partly counterbalanced by water stress ($\overline{Y_{\mathrm{W_{scale}}}}$). Cloudy days are as well characterized by a combined temperature-radiation control, but with radiation exerting stronger influence during daytime. At 9 km, radiation anomalies are weaker on clear-sky days and temperature effects are as well partly compensated by $\overline{Y_{W_{\mathrm{scale}}}}$, whereas under cloudy/rainy conditions both temperature and radiation contribute substantially, while the counterbalancing of $\overline{Y_{W_{\mathrm{scale}}}}$ reduces.

For R_{eco}, no perturbation analysis is required since its analytical temperature sensitivity $\frac{\partial R_{eco}}{\partial T_{2m}}$ is explicitly given by Eq. (7), which implies that temperature is the primary driver of ecosystem respiration. Consequently, the observed resolution-driven differences in R_{eco} can be attributed mostly to T_{2m}, while differences from the parameters α and β, have a domain dependent static contribution.

4 Discussion

This study examines real-case Alpine simulations to assess how grid spacing and parameter optimization affect modeled CO_2 fluxes over complex mountainous terrain. By comparing WRF-VPRM runs at 1, 9 and 54 km horizontal grid spacing and

https://doi.org/10.5194/egusphere-2026-939
Preprint. Discussion started: 8 May 2026

evaluating site-level, regional and default parameter sets, contributions of input variables at different resolutions and biases from parameterization effects are revealed.

Validation against five Alpine FLUXNET sites shows that site-specific (SITE) parameter sets for VPRM improve local performance relative to the domain wide optimization (ALPS) and WRF default parameter values (DF) as listed in Appendix D (Table D5). WRF near-surface temperature exhibits a systematic cold bias, indicating generally colder WRF conditions across the evaluation domain. Among the tested configurations, the SITE parameter set shows the most consistent overall behaviour, with strong performance for GPP and a nearly unbiased representation of ecosystem respiration, suggesting that site-specific optimization of VPRM parameters, including the optimum temperature (T_{opt}), compensates for the WRF cold bias. The DF parameter set performs comparatively well for NEE. However, this emerges from compensating errors in GPP and R_{eco} rather than from an improved representation of the underlying processes. ALPS as well exhibits intermediate performance, characterized by enhanced photosynthetic uptake combined with an unbiased respiration term, such that NEE is overestimated.

The fact that SITE performs better than ALPS supports the findings of Groenendijk et al. (2011), who demonstrated that parameters derived at the site-year level yield the highest predictive skill, whereas aggregation into broader classes such as PFT or climate groups only marginally improves flux representation. In the present case, mountainous terrain implies further challenges originating from systematic biases of nighttime flux uncertainties and from advection and storage under low turbulence, which limit the reliability of parameter estimation (Aubinet et al., 2010; Platter et al., 2024). As a consequence parameter optimization in the Alpine region has additional challenges due to scarcity and complexity of sites, yet the present study applies the state-of-the-art optimization strategy of Ranit et al. (2025) to obtain the ALPS parameters. In summary, regionally optimized parameters in the VPRM model for the 'Alpine region', based on the available 19 sites, do not produce a more accurate NEE than the reference (DF) parameters. However, It remains to be investigated whether this is the result of the 'case study' approach adopted here (only 24 days simulated), or of the site-to-site variability in complex terrain. If it is a matter of complex mountainous terrain, this further raises the question whether the VPRM parameterization itself needs to be extended with a terrain-specific component or, alternatively, it is merely the meteorological input. For the latter, however, turbulence characteristics and near-surface exchange processes in complex terrain must first be better understood (Rotach et al., 2022).

Coarser grid spacing generally enhances CO_2 uptake relative to the 1 km reference under clear-sky conditions, while the sign inverts under cloudy and rainy conditions, with substantially larger deviations at 54 km (Table 1). Hence, NEE responds more sensitively to grid spacing under cloudy/rainy conditions. Nevertheless, these resolution-driven differences are systematic, with consistent sign and spatial patterns linked to temperature and radiation differences, as well as biases from satellite-derived vegetation indices. The approximate yearly NEE of WRF-VPRM reported in the last row of Table 1 is based on 24 representative days and should be interpreted as a first-order estimate (Sect. 3.1), the sample is biased toward stronger carbon uptake by approximately 20% relative to full-year FLUXNET observations.

For ALPS and DF at 9 km grid spacing, the difference in yearly NEE to their respective 1 km simulations is minor, while variations between the two parameter sets are more pronounced, implying that parameter choices exert a stronger influence than grid spacing at this scale. In contrast, for ALPS parameters at 54 km grid spacing, the impact of grid spacing on yearly NEE substantially exceeds the difference between the ALPS and DF parameters. Conversely, the effects of decreasing grid spacing

https://doi.org/10.5194/egusphere-2026-939
Preprint. Discussion started: 8 May 2026

and parameter selection are of similar magnitude for the DF configuration. Taken together, these findings indicate that grid spacing is the dominant source of uncertainty at coarse scales, whereas at finer scales uncertainties related to parameterization become comparatively more relevant.

The apparent agreement in domain-average NEE between CAMS and the DF simulations (Figs. 5(e) and 7(e)) reflects offsetting biases: CAMS relies on a different biosphere model with a different seasonal cycle, and has large systematic offsets in T_{2m} and S↓ relative to WRF-VPRM, rather than accurate process representation.

From the linear perturbation analysis, temperature and radiation emerge as the dominant controls on GPP differences between coarse and fine resolution in the atmospheric model. Topographic smoothing and altered slope-aspect exposure systematically modify the surface energy balance (Destro et al., 2026), amplifying radiation and temperature anomalies that strongly affect Δ_{res}GPP. Vegetation and water-stress scalars, together with temperature, induce systematic and sign-consistent biases that mirror topographic variability. This demonstrates that structural biases arising from coarser resolution are not random but follow predictable spatial patterns governed by terrain characteristics. LSWI and EVI from satellite data, exhibit systematic biases which are dependent on the model domain and the grid spacing and therefore could potentially be bias-corrected. Temperature derivatives may make use of extrapolated temperatures and estimate NEE deviations arising from elevation differences, while for large temperature differences an extrapolation should be further refined when Δ_{res}T is exceeding T_{opt} (Sect. 2.4.3). In addition, radiation corrections accounting for slope and aspect could be calculated using high-resolution topography.

A more advanced biospheric model should be considered for future work, with explicit stomatal conductance responding to VPD and CO_2 (Cao et al., 2025) and plant acclimation that shifts the photosynthetic optimum to ambient temperatures at high altitudes (Wang et al., 2017a; Chen et al., 2023). Together with the pyVPRM framework (Glauch et al., 2025), which can ingest Sentinel-2 vegetation indices at up to 20 m grid spacing, such improvements would better represent subgrid heterogeneity in structurally diverse alpine landscapes.

A feasible approach to reduce structural resolution effects is a subgrid-scale flux parameterization that resolves terrain-vegetation interactions below the atmospheric model grid (O(10–100 km)). The key inputs are high-resolution topography for slope- and aspect-corrected radiation and lapse-rate temperature interpolation, high resolution satellite vegetation indices, and a biologically realistic GPP–R_{eco} scheme including VPD sensitivity and thermal acclimation. The resulting subgrid fluxes would be aggregated to the coarse atmospheric grid, improving not only CO_2 exchange but also transpiration and boundary-layer humidity in coupled land-atmosphere simulations.

5 Conclusion

This study applies WRF-VPRM to the European Alps to examine how grid spacing and parameter choice affect biospheric CO_2 exchange in complex terrain. The five questions raised in the Introduction are answered in turn.

(Q1) Coarser grids systematically bias CO_2 uptake, with a direction that depends on meteorological conditions. Under clear-sky conditions, uptake is slightly enhanced at coarser grid spacing relative to the 1 km reference, with NEE biases of 7% at 9 km (4% for DF) and 2% at 54 km (2% for DF). Under cloudy and rainy conditions the sign reverses, with coarser grids producing

https://doi.org/10.5194/egusphere-2026-939
Preprint. Discussion started: 8 May 2026

weaker uptake; the biases reach 12% at 9 km (8% for DF) and 68% at 54 km (43% for DF). These opposing responses prevent simple bias correction and underscore the need for high-resolution representation.

(Q2) At fine horizontal grid spacing (O(10 km)), parameter choice is the dominant source of uncertainty in the approximate yearly NEE: grid spacing changes annual NEE by only 2% for ALPS and 0% for DF at 9 km, whereas the difference from ALPS and DF parameters amounts to 15%. At coarse grid spacing (O(100 km)), the loss of spatial detail becomes the dominant source of uncertainty, with resolution-induced deviations of 17% for ALPS and 13% for DF at 54 km, exceeding the parameter effect of 8%.

(Q3) Validation against five Alpine FLUXNET sites shows that site-specific parameters perform best overall. The DF configuration achieves comparatively good NEE through compensating errors in GPP and ecosystem respiration, reflecting physically inconsistent flux components rather than accurate process representation. Comparison with CAMS confirms that WRF-VPRM results fall within a realistic range for the annual carbon budget, despite differences in seasonal cycle and meteorological drivers.

(Q4) Temperature is the primary physical driver of resolution-induced differences, explaining 35–42% of GPP biases and 71–85% of R_{eco} biases across grid spacings and parameter sets. Radiation accounts for most of the remaining GPP variance, while satellite-derived vegetation indices and water stress add smaller but systematic contributions, reflecting the resolution-dependent structure of the underlying satellite data.

(Q5) Although continuous annual simulations are required for a more robust assessment, the spatially coherent structure of temperature- and radiation-driven biases indicates clear potential for developing subgrid-scale corrections. Such parameterizations could explicitly resolve terrain-vegetation interactions to improve biospheric CO_2 exchange representation in coarse-resolution climate models.

Code and data availability. The full workflow for the WRF-VPRM simulations, including pre-processing, parameter optimization, and post-processing scripts, is available and in the WRF_VPRM_inComplexTopo repository (tag v0.1) at https://github.com/Matthias-Reif-PhD/WRF_VPRM_inComplexTopo and on Zenodo with additional sample data from WRF output: https://doi.org/10.5281/zenodo.19997546 (Reif, 2026). Data processing scripts are specific to the LEO5 cluster of UIBK that has been used to calculate the results. The modified WRF-VPRM source code, including the extensions for parallel execution of multiple parameter sets and the analytical temperature derivative implementations, is available at https://github.com/Matthias-Reif-PhD/WRF/tree/WRF-P and https://github.com/Matthias-Reif-PhD/WPS/tree/WRF-VPRM-CLC. The pyVPRM framework used for pre-processing and satellite data integration can be accessed at https://github.com/tglauch/pyVPRM. The meteorological initial and boundary conditions were obtained from the ECMWF ERA5 reanalysis (Hersbach et al., 2023) via the Copernicus Climate Data Store at https://cds.climate.copernicus.eu/. Land cover data were provided by the CORINE Land Cover 2018 dataset from the European Environment Agency, https://doi.org/10.2909/960998c1-1870-4e82-8051-6485205ebbac (European Union's Copernicus Land Monitoring Service information, 2020). Topographic information is based on SRTM 3-arc-second data, available from the U.S. Geological Survey SRTM archive: https://doi.org/10.5067/MEaSUREs/SRTM/SRTMGL3.003 (JPL, 2013). Vegetation indices (EVI and LSWI) were derived from the MODIS MOD09A1 Version 6.1 surface reflectance product: https://doi.org/https://doi.org/10.5067/MODIS/MOD09A1.061. CAMS global reanalysis data is accessible via the CAMS Atmosphere Data

https://doi.org/10.5194/egusphere-2026-939
Preprint. Discussion started: 8 May 2026

Store at https://atmosphere.copernicus.eu/data. Validation data from the FLUXNET2015 network were retrieved from the FLUXNET portal at https://doi.org/10.1038/s41597-020-0534-3 (Pastorello et al., 2020).

Appendix A: Optimization with differential evolution algorithm and NNSE

The parameter optimization employs the differential evolution (DE) algorithm from the python SciPy library (Storn and Price, 1997; Gommers et al., 2024), a population-based global optimization method particularly suited for nonlinear, non-differentiable and multi-modal objective functions. DE iteratively improves a population of parameter vectors by combining mutation, crossover, and selection operations. New candidate solutions are generated by adding the weighted difference between randomly selected parameter vectors to another vector, followed by recombination and selection based on the objective function value. This approach efficiently explores the parameter space and reduces the likelihood of convergence to local minima, making it well suited for calibrating the nonlinear VPRM response functions.

To evaluate model performance during optimization, a weighted normalized Nash-Sutcliffe efficiency (NNSE) metric is used. The NNSE, defined below, is a modified form of the classical Nash-Sutcliffe efficiency that normalizes values and applies an uncertainty-based weighting factor. The weighting term $\sigma_{\text{weight},t}$ assigns higher influence to each timestep of observation t with lower random uncertainty, thus enhancing the stability and reliability of the parameter estimation in the presence of measurement noise and data gaps common in FLUXNET eddy covariance time series (Ranit et al., 2025).

$$\text{NSE} = 1 - \frac{\sum_{t=1}^{\text{N}_t} \left(\sigma_{\text{weight},t} \times \left(\text{NEE}_{\text{FLUXNET},t} - \text{NEE}_{\text{VPRM},t}\right)\right)^2}{\sum_{t=1}^{\text{N}_t} \left(\sigma_{\text{weight},t} \times \left(\text{NEE}_{\text{FLUXNET},t} - \overline{\text{NEE}_{\text{FLUXNET},t}}\right)\right)^2} \tag{A1}$$

$$\text{NNSE} = \frac{1}{2 - \text{NSE}} \tag{A2}$$

$$\sigma_{\text{weight},t} = 1 - \frac{\sigma_t - \min(\sigma)}{\max(\sigma) - \min(\sigma)} \tag{A3}$$

Appendix B: Decomposition of GPP differences with linear perturbation analysis

For each grid-cell, the goal is to determine how much each driver in the GPP equation (2) contributes to the total GPP difference between model grid spacings $\Delta_{\text{res}}\text{GPP} = \text{GPP}_{coarse} - \text{GPP}_{1\text{km}}$, where Δ_{res} indicates the difference between coarse and 1 km grid spacing. This method is formulated as a linear inverse problem, where the sensitivities with respect to the drivers are inferred from the observed differences using a least-squares approach (e.g. Tarantola, 2005).

https://doi.org/10.5194/egusphere-2026-939
Preprint. Discussion started: 8 May 2026

For a single grid-cell, the differences of the drivers are collected into the vector

$$\Delta_{\text{res}}\mathbf{x} = \begin{bmatrix} \Delta_{\text{res}}\lambda \\ \Delta_{\text{res}}T_{\text{scale}} \\ \Delta_{\text{res}}\text{W}_{\text{scale}} \\ \Delta_{\text{res}}\text{P}_{\text{scale}} \\ \Delta_{\text{res}}\text{RAD} \\ \Delta_{\text{res}}\text{EVI} \end{bmatrix}, \tag{B1}$$

where

$$\Delta_{\text{res}}x_i = x_{i,\text{coarse}} - x_{i,1\,\text{km}} \qquad x_i \in \{\lambda, T_{\text{scale}}, \text{W}_{\text{scale}}, \text{P}_{\text{scale}}, \text{RAD}, \text{EVI}\}. \tag{B2}$$

for all grid-points. The change in GPP at each grid-point is assumed to depend linearly on the drivers, as shown already in Eq. (10)

$$\Delta_{\text{res}}\mathbf{GPP} \approx \sum_i \frac{\partial \text{GPP}}{\partial x_i}\Delta_{\text{res}}x_i + \varepsilon. \tag{B3}$$

For the entire domain, all grid-points are stacked into a matrix $\mathbf{D}$:

$$\mathbf{D} = \begin{bmatrix} \Delta_{\text{res}}\lambda_1 & \Delta_{\text{res}}T_1 & \Delta_{\text{res}}W_1 & \Delta_{\text{res}}P_1 & \Delta_{\text{res}}RAD_1 & \Delta_{\text{res}}EVI_1 \\ \Delta_{\text{res}}\lambda_2 & \Delta_{\text{res}}T_2 & \Delta_{\text{res}}W_2 & \Delta_{\text{res}}P_2 & \Delta_{\text{res}}RAD_2 & \Delta_{\text{res}}EVI_2 \\ \vdots & \vdots & \vdots & \vdots & \vdots & \vdots \\ \Delta_{\text{res}}\lambda_N & \Delta_{\text{res}}T_N & \Delta_{\text{res}}W_N & \Delta_{\text{res}}P_N & \Delta_{\text{res}}RAD_N & \Delta_{\text{res}}EVI_N \end{bmatrix}, \tag{B4}$$

where N is the number of valid grid-points. Each row corresponds to a grid-point, each column to a driver.

The equation system

$$\mathbf{DA} \approx \Delta_{\text{res}}\mathbf{GPP}, \tag{B5}$$

is solved, for the vector $\Delta_{\text{res}}\mathbf{GPP}$, representing differences of GPP for each grid-point and for the sensitivity vector

$$\mathbf{A} = \begin{bmatrix} \frac{\partial \text{GPP}}{\partial \lambda} \\ \frac{\partial \text{GPP}}{\partial T_{\text{scale}}} \\ \frac{\partial \text{GPP}}{\partial \text{W}_{\text{scale}}} \\ \frac{\partial \text{GPP}}{\partial \text{P}_{\text{scale}}} \\ \frac{\partial \text{GPP}}{\partial \text{RAD}} \\ \frac{\partial \text{GPP}}{\partial \text{EVI}} \end{bmatrix}. \tag{B6}$$

Since there are usually more grid-points than drivers ($N \gg 6$), this system is over-determined. In general, no exact solution exists.

https://doi.org/10.5194/egusphere-2026-939
Preprint. Discussion started: 8 May 2026

The least-squares solution minimizes the sum of squared differences between the GPP differences from the two grid spacings:

$$\min_{\mathbf{A}} \|\Delta_{\text{res}}\mathbf{GPP} - \mathbf{DA}\|^2. \tag{B7}$$

By setting the gradient of this cost function with respect to $\mathbf{A}$ to zero, one obtains

$$\mathbf{D}^T\mathbf{DA} = \mathbf{D}^T\Delta_{\text{res}}\mathbf{GPP}. \tag{B8}$$

Solving for $\mathbf{A}$ gives

$$\mathbf{A} = (\mathbf{D}^T\mathbf{D})^{-1}\mathbf{D}^T\Delta_{\text{res}}\mathbf{GPP} = \mathbf{D}^+\Delta_{\text{res}}\mathbf{GPP}, \tag{B9}$$

where $\mathbf{D}^+$ denotes the Moore-Penrose pseudoinverse of $\mathbf{D}$ (Penrose, 1955), which provides the best-fit sensitivities in a least-squares sense. This solution distributes the contributions of each driver in a way that minimizes the overall squared residual across all grid-points, producing the optimal linear decomposition of $\Delta_{\text{res}}\mathbf{GPP}$.

If some drivers are highly correlated, the matrix $\mathbf{D}^T\mathbf{D}$ may be nearly singular. To avoid numerical instability, a small ridge term $\alpha\mathbf{I}$ is added:

$$\mathbf{A} = (\mathbf{D}^T\mathbf{D} + \alpha\mathbf{I})^{-1}\mathbf{D}^T\Delta_{\text{res}}\mathbf{GPP}. \tag{B10}$$

Once $\mathbf{A}$ is obtained, the contribution of each driver at each grid-point is computed as

$$Y_{x_i} = \Delta_{\text{res}} x_i \frac{\partial \text{GPP}}{\partial x_i} \qquad x_i \in \{\lambda, T_{\text{scale}}, \text{W}_{\text{scale}}, \text{P}_{\text{scale}}, \text{RAD}, \text{EVI}\} \tag{B11}$$

and substituting Eq. (B3) the residual is

$$\varepsilon = \Delta_{\text{res}}\mathbf{GPP} - \sum_{x_i} Y_{x_i}. \tag{B12}$$

This formulation ensures that each grid-point's GPP difference is decomposed into contributions from the drivers while preserving spatial information. The averaging of Y_{x_i} over all grid-points then provides domain-mean contributions (Eq. (15)).

Appendix C: Temperature derivatives of biospheric Fluxes

To evaluate the temperature sensitivity of biospheric CO_2 fluxes in the WRF-VPRM model, the partial derivatives of photosynthesis or gross primary production (GPP) and ecosystem respiration (R_{eco}) with respect to the 2-meter air temperature field (T_{2m}) are determined. The total GPP for all vegetation types per grid cell is defined in Eq. (11). To simplify the notation it is shown for all PFT (without the subscript v). The differences in T_{scale} (Eq. (4)) are divided into

$$a_1 = T_{2\text{m}} - T_{\min}, \quad a_2 = T_{2\text{m}} - T_{\max}, \quad a_3 = T_{2\text{m}} - T_{\text{opt}} \tag{C1}$$

https://doi.org/10.5194/egusphere-2026-939
Preprint. Discussion started: 8 May 2026

while the constraints are

$$T_{\text{scale}} = \begin{cases} \dfrac{a_1 a_2}{a_1 a_2 - a_3^2}, & \text{if } a_1 \geq 0 \text{ and } a_2 \leq 0 \text{ and } T_{\text{scale}} \geq 0 \\ 0, & \text{otherwise.} \end{cases} \tag{C2}$$

By applying the product rule and the quotient rule

$$\frac{\partial T_{\text{scale}}}{\partial T_{2\text{m}}} = \begin{cases} \dfrac{(a_1 + a_2)(a_1 a_2 - a_3^2) - a_1 a_2 \left((a_1 + a_2) - 2a_3\right)}{(a_1 a_2 - a_3^2)^2}, & \text{if } T_{\text{scale}} \geq 0 \\ 0, & \text{otherwise} \end{cases} \tag{C3}$$

is obtained, which results in

$$\frac{\partial \text{GPP}}{\partial T_{2\text{m}}} = \lambda \frac{\partial T_{\text{scale}}}{\partial T_{2\text{m}}} \text{P}_{\text{scale}} \text{W}_{\text{scale}} \, \text{RAD} \cdot \text{EVI}. \tag{C4}$$

The ecosystem respiration for all PFT is

$$\text{R}_{\text{eco}} = \alpha T_{2\text{m}} + \beta \tag{C5}$$

the derivative of R_{eco} with respect to $T_{2\text{m}}$ is

$$\frac{\partial \text{R}_{\text{eco}}}{\partial T_{2\text{m}}} = \alpha. \tag{C6}$$

Appendix D: Additional tables

D1 CORINE to VPRM remapping table

Table D1 presents the remapping scheme used to convert the 44 CORINE land cover categories to the eight VPRM plant functional types (PFT).

The raw CORINE data were reprojected and resampled to the WRF grid using the programs "gdalwarp" and "gdal_translate", ensuring consistent spatial alignment and grid spacing with the model domain.

https://doi.org/10.5194/egusphere-2026-939
Preprint. Discussion started: 8 May 2026

Table D1. Remapping of CORINE to VPRM

CORINE ID$_A$	CORINE ID$_B$	CORINE Vegetation Type	VPRM ID	VPRM Vegetation Type
1	111	Continuous Urban Fabric	8	Others
2	112	Discontinuous Urban Fabric	8	Others
3	121	Industrial or Commercial Units	8	Others
4	122	Road and Rail Networks	8	Others
5	123	Port Areas	8	Others
6	124	Airports	8	Others
7	131	Mineral Extraction Sites	8	Others
8	132	Dump Sites	8	Others
9	133	Construction Sites	8	Others
10	141	Green Urban Areas	8	Others
11	142	Sport and Leisure Facilities	8	Others
12	211	Non-irrigated Arable Land	6	Croplands
13	212	Permanently Irrigated Land	6	Croplands
14	213	Rice Fields	6	Croplands
15	221	Vineyards	6	Croplands
16	222	Fruit Trees and Berry Plantations	6	Croplands
17	223	Olive Groves	6	Croplands
18	231	Pastures	7	Grasslands
19	241	Annual Crops Associated with Permanent Crops	6	Croplands
20	242	Complex Cultivation Patterns	6	Croplands
21	243	Land Principally Occupied by Agriculture	6	Croplands
22	244	Agro-forestry areas	6	Croplands
23	311	Broad-leaved Forest	2	Deciduous Broadleaf Forest
24	312	Coniferous Forest	1	Evergreen Needleleaf Forest
25	313	Mixed Forest	3	Mixed Forests
26	321	Natural Grasslands	7	Grasslands
27	322	Moors and Heathland	4	Shrublands
28	323	Sclerophyllous Vegetation	4	Shrublands
29	324	Transitional Woodland-Shrub	3	Mixed Forests
30	331	Beaches, Dunes, Sands	8	Others
31	332	Bare Rocks	8	Others
32	333	Sparsely Vegetated Areas	8	Others
33	334	Burnt Areas	8	Others
34	335	Glaciers and Perpetual Snow	8	Others
35	411	Inland Marshes	8	Others
36	412	Peat Bogs	8	Others
37	421	Salt marshes	8	Others
38	422	Salines	8	Others
39	423	Intertidal flats	8	Others
40	511	Water courses	8	Others
41	512	Water bodies	8	Others
42	521	Coastal lagoons	8	Others
43	522	Estuaries	8	Others
44	523	Sea and Ocean	8	Others

https://doi.org/10.5194/egusphere-2026-939
Preprint. Discussion started: 8 May 2026

D2 VPRM parameter sets and performance

Table D2 provides site information for the FLUXNET locations used in parameter optimization, including 15 sites located within the Alpine region (latitudes 44–50 N and longitudes 5–17 E) and four additional European sites included to account for underrepresented PFT.

Tables D3 and D4, list the PFT-specific parameter values for the reference (DF), Alpine-optimized (ALPS), and site-specific (SITE) VPRM parameter sets. The potential light-use efficiency parameter λ listed in Tables D3 and D4 is given with a positive sign. This convention ensures that the resulting GPP is mathematically positive for CO_2 uptake, consistent with the notation used throughout the manuscript. In contrast, the WRF implementation stores λ with a negative sign, as GPP is defined internally as a negative flux in WRF.

Table D5 (MB and MAE) and D7 (RMSE and R^2) summarize the detailed metrics for the 1 km simulation validated against FLUXNET measurements for all three parameter sets across five Alpine sites.

Table D2. Site information for the Alpine sites

Site	Country	PFT	Latitude	Longitude	Elevation (m)	Site years of data
AT-Neu	Austria	GRA	47.1167	11.3175	970	11
CH-Cha	Switzerland	GRA	47.2102	8.4104	393	10
CH-Dav	Switzerland	ENF	46.8153	9.8559	1639	18
CH-Fru	Switzerland	GRA	47.1158	8.5378	982	10
CH-Lae	Switzerland	MF	47.4781	8.365	689	11
CH-Oe1	Switzerland	GRA	47.2858	7.7319	450	7
CH-Oe2	Switzerland	CRO	47.2863	7.7343	452	11
DE-Lkb	Germany	ENF	49.0996	13.3047	1308	5
IT-Isp	Italy	DBF	45.8126	8.6336	210	2
IT-La2	Italy	ENF	45.9542	11.2853	1350	3
IT-Lav	Italy	ENF	45.9562	11.2813	1353	12
IT-MBo	Italy	GRA	46.0147	11.0458	1550	11
IT-PT1	Italy	DBF	45.2009	9.0610	60	3
IT-Ren	Italy	ENF	46.5869	11.4337	1730	15
IT-Tor	Italy	GRA	45.8444	7.5781	2160	7
DE-Hai [1]	Germany	DBF	51.0792	10.4530	430	13
DE-Kli [1]	Germany	CRO	50.8929	13.5225	478	11
FR-Fon [1]	France	DBF	48.4764	2.7801	103	10
FR-Gri [1]	France	CRO	48.8442	1.9519	125	11

https://doi.org/10.5194/egusphere-2026-939
Preprint. Discussion started: 8 May 2026

Table D3. VPRM parameter sets calibrated specifically for domain d01 for the Alps (ALPS) compared to default values from WRF for Europe (DF) by plant functional type (PFT). Both sets were calibrated directly with assuming shortwave downward radiation is the photosynthetically absorbed radiation (PAR).

	ENF	DBF	MF	SHB	SAV	CRO	GRA	OTH
$T_{\text{opt, ALPS}}$	14.25	23.58	17.44	20.0	20.0	22.0	15.88	0.0
$T_{\text{opt,DF}}$	20.0	20.0	20.0	20.0	20.0	22.0	18.0	0.0
$\text{PAR}_{0,\text{ ALPS}}$	207.69	183.80	240.39	363.0	682.0	364.15	284.87	0.0
$\text{PAR}_{0,\text{ DF}}$	270.2	271.4	236.6	363.0	682.0	690.3	229.1	0.0
λ_{ALPS}	0.467	0.361	0.248	0.087	0.114	0.230	0.771	0.0
λ_{DF}	0.308	0.196	0.286	0.087	0.114	0.135	0.175	0.0
α_{ALPS}	0.175	0.235	0.202	0.024	0.005	0.234	0.390	0.0
α_{DF}	0.180	0.150	0.226	0.024	0.005	0.170	0.088	0.0
β_{ALPS}	1.702	0.887	2.734	0.0	0.0	1.050	1.474	0.0
β_{DF}	0.880	0.823	0.432	0.0	0.0	-0.014	0.584	0.0

Table D4. Site-specific Alpine parameters (SITE) and optimized values for 2012, comprising plant functional type (PFT), site location (latitude and longitude in degrees, elevation in m), and physiological parameters $T_{\text{opt, SITE}}$ (°C), $\text{PAR}_{0,\text{ SITE}}$ (μmol m^{-2} s^{-1}), α_{SITE} (μmol m^{-2} s^{-1} $°\text{C}^{-1}$), β_{SITE} (μmol m^{-2} s^{-1}) and λ_{SITE} (μmol m^{-2} s^{-1}).

Site	PFT	Latitude	Longitude	AMSL	$T_{\text{opt, SITE}}$	$\text{PAR}_{0,\text{ SITE}}$	α_{SITE}	β_{SITE}	λ_{SITE}
AT-Neu	GRA	47.1167	11.3175	970	13.0	268.06	0.5	4.101	0.722
CH-Dav	ENF	46.8153	9.8559	1639	9.7	418.39	0.285	0.545	0.236
IT-Lav	ENF	45.9562	11.2813	1353	14.5	468.82	0.135	0.010	0.227
IT-MBo	GRA	46.0147	11.0458	1550	16.3	445.60	0.404	2.454	0.549
IT-Ren	ENF	46.5869	11.4337	1730	11.9	455.34	0.107	1.829	0.213

Table D5. Evaluation against FLUXNET measurements ($\overline{\text{FLX}}$) of modeled values at 1 km for different parameter sets SITE, ALPS and DF. Mean bias (MB) and mean absolute error (MAE, shown in brackets) for $T_{2\text{m}}$ (°C), NEE (μmol m^{-2} s^{-1}), GPP in (μmol m^{-2} s^{-1}) and R_{eco} (μmol m^{-2} s^{-1}) of five Alpine sites in 2012 on 12 clear-sky days and 12 cloudy/rainy days. Best MB and MAE per flux type and site are highlighted in bold.

		$T_{2\text{m}}$		GPP				R_{eco}				NEE			
Site	PFT	$\overline{\text{FLX}}$	WRF	$\overline{\text{FLX}}$	SITE	ALPS	DF	$\overline{\text{FLX}}$	SITE	ALPS	DF	$\overline{\text{FLX}}$	SITE	ALPS	DF
AT-Neu	83% GRA	7.62	-1.79 (3.54)	7.96	-3.28 (**3.92**)	**1.01** (4.87)	-5.84 (5.95)	8.22	**-4.70** (**4.70**)	-4.74 (4.74)	-7.14 (7.14)	1.06	-2.21 (**5.10**)	-6.55 (8.02)	**-2.09** (6.51)
CH-Dav	94% ENF	7.85	-4.37 (4.51)	3.47	0.79 (2.65)	0.90 (2.74)	**-0.20** (**2.08**)	2.41	0.75 (1.48)	**-0.07** (**1.37**)	-0.91 (1.37)	-0.99	**-0.11** (3.42)	-1.05 (3.74)	-0.78 (**3.00**)
IT-Lav	100% ENF	9.70	-1.75 (2.06)	6.45	**0.20** (2.64)	0.92 (2.99)	-0.63 (**2.37**)	1.01	2.69 (2.69)	2.08 (2.08)	**1.30** (**1.30**)	-5.47	2.52 (3.88)	**1.19** (3.98)	1.95 (**3.18**)
IT-MBo	91% GRA	7.69	-0.57 (1.63)	4.48	**-0.27** (**1.73**)	3.30 (4.00)	-2.58 (2.64)	4.19	0.67 (1.51)	**-0.00** (**1.36**)	-2.90 (2.90)	-0.30	0.95 (2.98)	-3.29 (4.98)	**-0.31** (**2.83**)
IT-Ren	95% ENF	7.72	-1.45 (2.06)	4.62	**0.08** (2.27)	1.08 (2.69)	-0.27 (**2.17**)	2.21	0.67 (0.86)	0.64 (0.84)	**-0.25** (**0.64**)	-2.40	0.58 (2.53)	-0.45 (2.86)	**0.01** (**2.41**)
Mean	–	8.12	-1.99 (2.76)	5.40	**-0.50** (**2.64**)	1.44 (3.46)	-1.90 (3.04)	3.61	**0.02** (2.25)	-0.42 (**2.08**)	-1.98 (2.67)	-1.62	0.35 (**3.58**)	-2.03 (4.71)	**-0.24** (3.59)

https://doi.org/10.5194/egusphere-2026-939
Preprint. Discussion started: 8 May 2026

Table D6. Yearly mean FLUXNET observations and corresponding values derived from 24 sampled days (12 clear-sky and 12 cloudy/rainy, shown in brackets) for T_{2m} (°C), SWin (W m^{-2}), GPP (μmol m^{-2} s^{-1}), R_{eco} (μmol m^{-2} s^{-1}), and NEE (μmol m^{-2} s^{-1}) in 2012 at 19 ALPS sites. The final row shows the multi-site mean. The four sites CH-Oe1, IT-Isp, IT-La2 and IT-PT1 have no measurements in 2012. Sites with [1] are inside domain d03 and with [2] outside but close to domain d01.

Site	T_{2m}	SW_{in}	GPP	R_{eco}	NEE
AT-Neu [1]	6.71 (7.62)	137.42 (188.44)	6.03 (7.96)	7.04 (8.22)	1.26 (1.06)
IT-MBo [1]	5.57 (7.69)	162.35 (198.34)	4.14 (4.48)	4.18 (4.19)	0.07 (-0.30)
CH-Dav [1]	4.08 (7.85)	153.10 (197.52)	3.15 (3.47)	2.13 (2.41)	-1.05 (-0.99)
IT-Lav [1]	7.33 (9.70)	158.26 (196.60)	6.17 (6.45)	0.87 (1.01)	-5.42 (-5.47)
IT-Ren [1]	4.84 (7.72)	162.23 (207.53)	3.95 (4.62)	2.30 (2.21)	-1.77 (-2.40)
IT-Tor	3.45 (6.70)	165.65 (190.92)	2.15 (2.42)	2.17 (2.36)	0.12 (-0.05)
CH-Cha	9.52 (11.02)	142.94 (193.22)	4.95 (6.97)	5.70 (7.01)	0.90 (0.14)
CH-Fru	7.60 (10.90)	140.32 (210.71)	5.56 (6.59)	4.83 (5.87)	-0.45 (-0.46)
CH-Lae	7.77 (11.26)	138.34 (194.02)	5.24 (5.93)	3.16 (3.74)	-2.08 (-2.18)
CH-Oe2	9.15 (10.85)	141.54 (190.96)	4.06 (4.82)	3.41 (3.94)	-0.60 (-0.64)
DE-Lkb	4.77 (9.25)	131.18 (175.58)	1.48 (1.76)	2.10 (2.44)	0.69 (0.61)
DE-Hai [2]	8.28 (11.99)	123.62 (161.28)	4.18 (4.96)	2.78 (3.18)	-1.38 (-1.58)
DE-Kli [2]	7.51 (10.79)	133.61 (170.05)	1.81 (2.08)	1.97 (2.03)	0.18 (-0.05)
FR-Fon [2]	11.50 (13.60)	131.60 (146.04)	4.73 (4.73)	3.19 (3.70)	-1.40 (-0.77)
FR-Gri [2]	10.74 (12.99)	133.18 (138.83)	3.27 (3.57)	2.22 (2.66)	-0.97 (-0.89)
Mean	7.25 (10.00)	143.69 (184.00)	4.06 (4.72)	3.20 (3.67)	-0.79 (-0.93)

Table D7. Evaluation against FLUXNET measurements of modeled values at 1 km for different parameter sets SITE, ALPS and DF. Root mean squared error (RMSE) and correlation coefficient (R^2, shown in brackets) for T_{2m} (°C), NEE (μmol m^{-2} s^{-1}), GPP (μmol m^{-2} s^{-1}) and R_{eco} (μmol m^{-2} s^{-1}) of five Alpine sites in 2012 on 12 clear-sky days and 12 cloudy/rainy days. Lowest RMSE and highest R^2 per flux type and site are highlighted in bold.

		T_{2m}	GPP			R_{eco}			NEE		
Site	PFT	WRF	SITE	ALPS	DF	SITE	ALPS	DF	SITE	ALPS	DF
AT-Neu	83% GRA	5.41 (0.71)	**8.06 (0.58)**	9.71 (0.40)	11.26 (0.19)	**5.83 (-0.16)**	5.88 (-0.18)	8.60 (-1.52)	**6.66 (0.56)**	11.51 (-0.31)	8.11 (0.35)
CH-Dav	94% ENF	5.15 (0.47)	5.30 (0.05)	5.45 (-0.01)	**3.94 (0.47)**	1.82 (0.43)	**1.66 (0.53)**	1.92 (0.36)	4.94 (-0.08)	5.89 (-0.53)	**4.41 (0.14)**
IT-Lav	100% ENF	2.77 (0.78)	4.82 (0.71)	5.43 (0.63)	**4.44 (0.75)**	2.91 (-6.05)	2.16 (-2.90)	**1.43 (-0.70)**	5.16 (0.62)	5.48 (0.58)	**4.82 (0.67)**
IT-MBo	91% GRA	2.25 (0.87)	**3.30 (0.81)**	9.37 (-0.52)	5.22 (0.53)	1.81 (0.62)	**1.63 (0.69)**	3.82 (-0.70)	**3.96 (0.60)**	9.95 (-1.54)	4.03 (0.58)
IT-Ren	95% ENF	2.75 (0.80)	4.33 (0.60)	5.24 (0.42)	**4.13 (0.64)**	1.09 (-0.07)	1.08 (-0.04)	**0.88 (0.31)**	4.12 (0.60)	4.86 (0.44)	**3.93 (0.64)**
Mean	–	3.66 (0.72)	**5.16 (0.55)**	7.04 (0.18)	5.80 (0.52)	2.69 (-1.05)	**2.48 (-0.38)**	3.33 (-0.45)	**4.97** (0.46)	7.54 (-0.27)	5.06 (**0.48**)

https://doi.org/10.5194/egusphere-2026-939
Preprint. Discussion started: 8 May 2026

D3 Abbreviations

Table D8 provides a complete list of abbreviations used throughout the manuscript.

Table D8: List of abbreviations and definitions

Abbreviations	Full Form
ALPS	Parameter set of Alpine sites used to optimize VPRM
AMSL	Above Mean Sea Level
CAMS	Copernicus Atmospheric Monitoring System
CORINE	Coordination of Information on the Environment land cover data
CRO	Cropland
DBF	Deciduous Broadleaf temperate Forest
DE	Differential Evolution
DF	Default parameter set of WRF-VPRM
ENF	Evergreen Needleleaf Forest
ERA5	ECMWF Reanalysis v5
EVI	Enhanced Vegetation Index
FLUXNET	A global network of eddy covariance towers that measure ecosystem fluxes
GFS	Global Forecast System
GPP	Gross Primary Production
GRA	Grassland
LSWI	Land Surface Water Index
MAE	Mean Absolute Error
MB	Mean Bias
MF	Mixed Forest
MODIS	Moderate Resolution Imaging Spectroradiometer
NEE	Net Ecosystem Exchange
NNSE	Normalized Nash-Sutcliffe Efficiency
PFT	Plant Functional Type
P-model	optimality-based photosynthesis model
R_{eco}	Ecosystem Respiration
RMSE	Root Mean Square Error
SAV	Savanna
SHB	Shrubland
SITE	Parameter set of Alpine sites in domain d03 used to optimize VPRM
SRTM	Shuttle Radar Topography Mission
STD_{TOPO}	standard deviation of subgrid-scale topography
T_{2m}	2 m air temperature
T_{opt}	photosynthetic optimum temperature
UTC	Coordinated Universal Time
u_*	Friction Velocity
VPD	Vapor Pressure Deficit
VPRM	Vegetation Photosynthesis and Respiration Model
VUT	Variable u_* Threshold
WRF	Weather Research and Forecasting model

https://doi.org/10.5194/egusphere-2026-939
Preprint. Discussion started: 8 May 2026

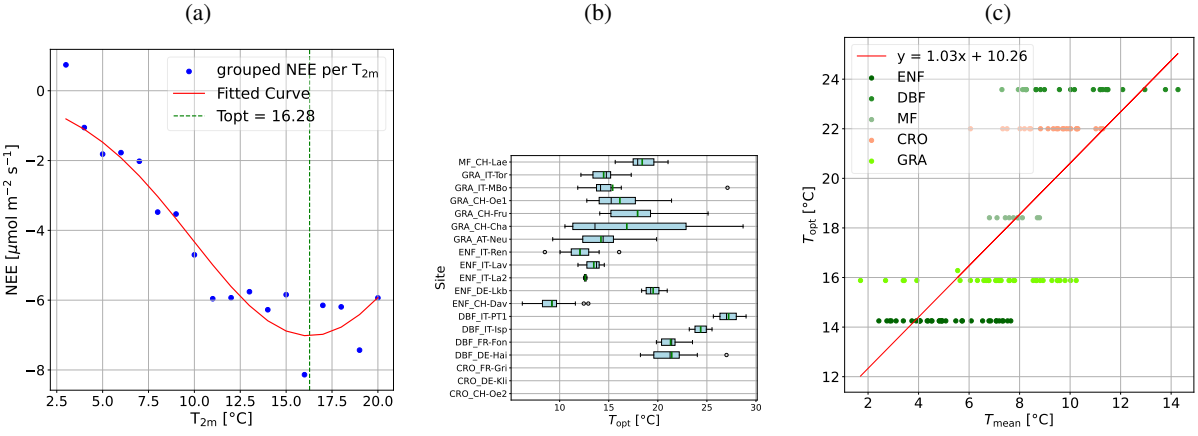

Figure E1. Panel (a) shows the Bell-shaped curve fitted to NEE data for the 2012 site-year at IT-Mbo to determine the optimum temperature (T_{opt}). Panel (b) shows the distribution of T_{opt} for all available site-years at each FLUXNET location (means in green lines, medians in thin black lines, 25–75 percentiles in blue bars, 5–95 percentiles with black lines and outliers in circles). Cropland (CRO) data did not yield useful values due to cutting events. Panel (c) shows the final obtained T_{opt} for five PFT correlated with their yearly mean temperatures per site (the default value of 22°C from WRF-VPRM is used for CRO).

Appendix E: Additional figures

E1 Optimum temperature

Figure E1 illustrates the methodology used to derive the plant functional type (PFT)-specific optimum temperature (T_{opt}) for the Alps, which partly accounts for varying altitudes and temperatures in the region. Figure E1(a) shows the process, which involves fitting a bell-shaped curve to binned NEE data from FLUXNET sites as a function of temperature to determine T_{opt} for a site-year. Figure E1(b) shows the distribution of T_{opt} for available site-years and correlates the final PFT-specific T_{opt} values with yearly mean temperatures per site (Fig. E1(c)). CRO does not result in useful values due to cutting events, hence the default value of 22°C from WRF-VPRM is used.

E2 FLUXNET sites for the Alps

This subsection includes validation figures (Figs. E2–E5) that display the mean diurnal cycles for the remaining four Alpine FLUXNET sites (AT-Neu, IT-Ren, CH-Dav, and IT-Lav). The figures validate model performance against observed CO_2 fluxes by comparing T_{2m}, GPP, R_{eco}, and NEE from the three VPRM parameter sets (SITE, ALPS, DF) and CAMS data, providing results analogous to those presented in Fig. 4.

https://doi.org/10.5194/egusphere-2026-939
Preprint. Discussion started: 8 May 2026

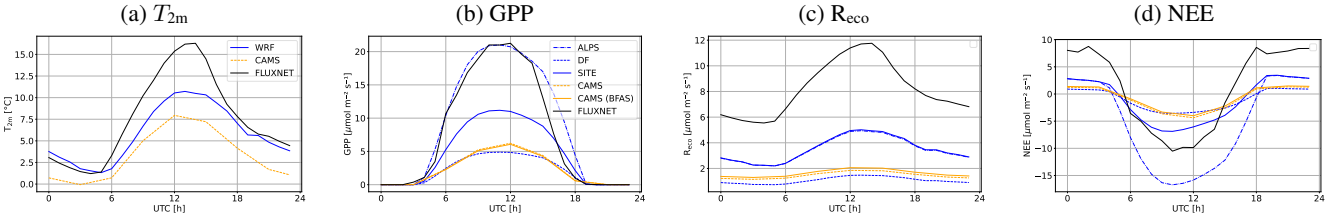

Figure E2. As Fig. 4 but for FLUXNET site Neustift in Austria (AT-Neu).

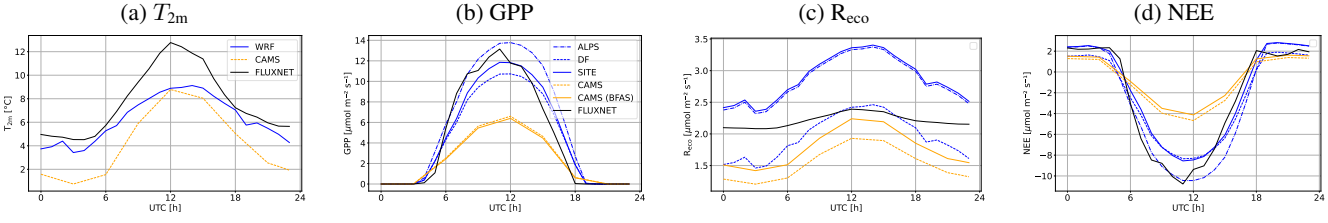

Figure E3. As Fig. 4 but for FLUXNET site Renon in Italy (IT-Ren).

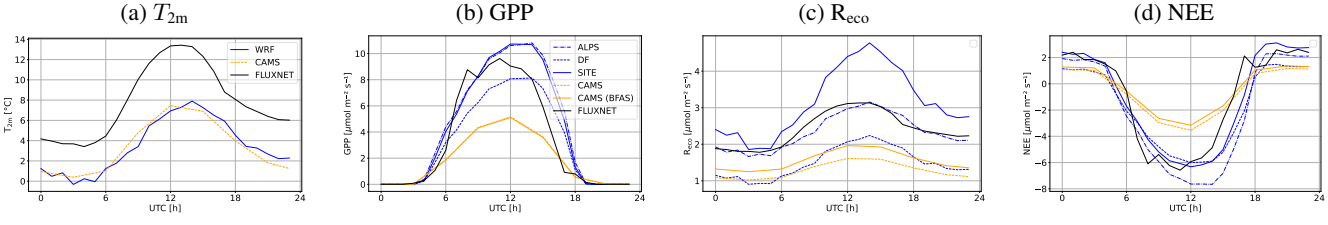

Figure E4. As Fig. 4 but for FLUXNET site Davos in Switzerland (CH-Dav).

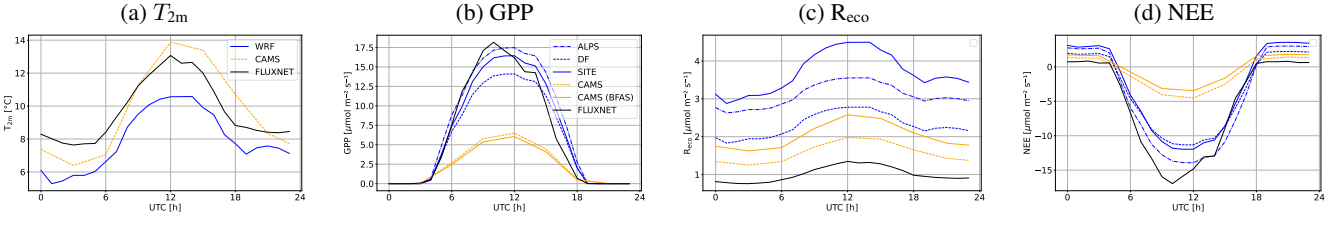

Figure E5. As Fig. 4 but FLUXNET site for Lavarone in Italy (IT-Lav).

https://doi.org/10.5194/egusphere-2026-939
Preprint. Discussion started: 8 May 2026

E3 Timeseries for domain averaged variables

This subsection presents comprehensive time series (Figs. E6–E15) of domain-averaged variables, including 2 m air temperature (T_{2m}), shortwave downward radiation ($S\downarrow$), gross primary production (GPP), ecosystem respiration (R_{eco}), and net ecosystem exchange (NEE). The time series are shown for both 12 clear-sky and 12 cloudy/rainy days during 2012, comparing simulations at 1 km, 9 km, and 54 km grid spacings using both ALPS and DF parameters, alongside averages of CAMS.

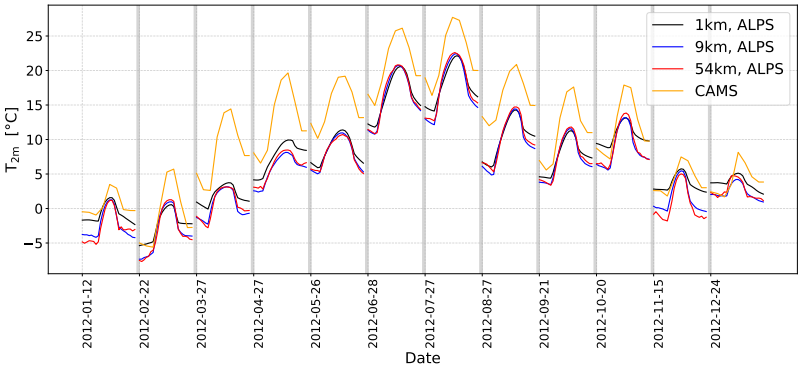

Figure E6. Timeseries for average 2 m air temperature (T_{2m}) over domain d03 on clear-sky days during 2012.

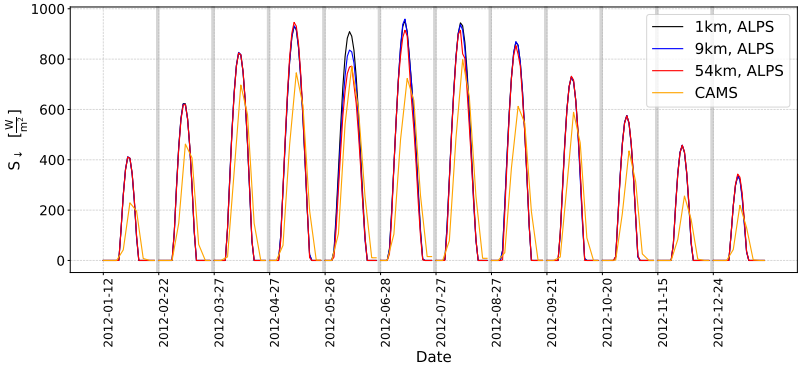

Figure E7. Timeseries for average shortwave downward radiation (S↓) over domain d03 on clear-sky days during 2012.

https://doi.org/10.5194/egusphere-2026-939
Preprint. Discussion started: 8 May 2026

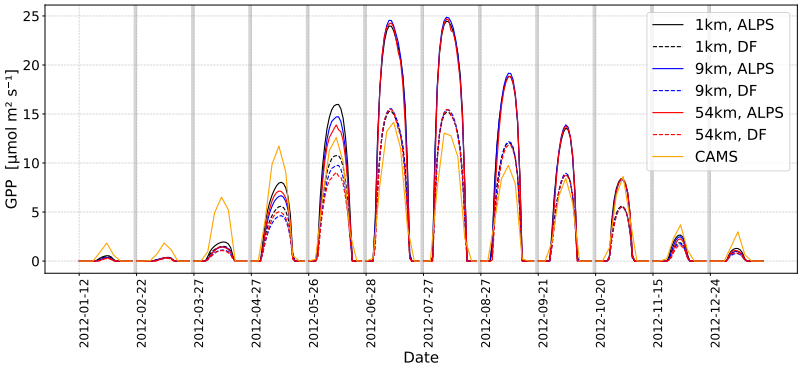

Figure E8. Timeseries for average gross primary production (GPP) over domain d03 on clear-sky days during 2012.

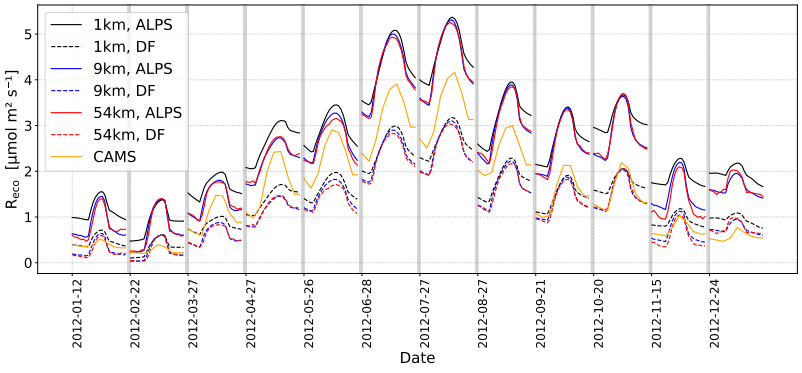

Figure E9. Timeseries for average ecosystem respiration (R_{eco}) over domain d03 on clear-sky days during 2012.

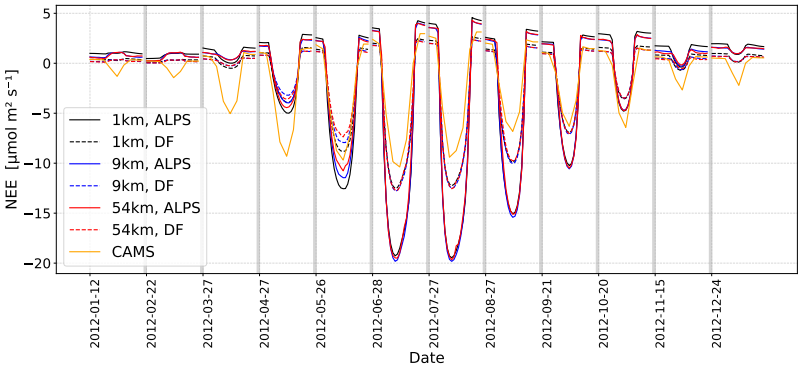

Figure E10. Time series of domain-averaged net ecosystem exchange (NEE) over domain d03 on clear-sky days during 2012.

https://doi.org/10.5194/egusphere-2026-939
Preprint. Discussion started: 8 May 2026

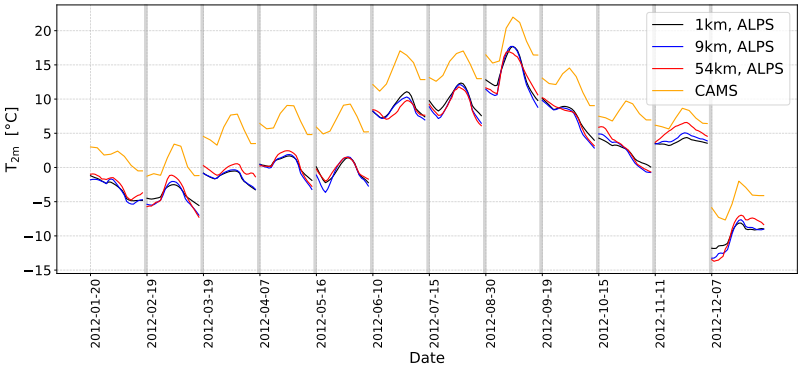

Figure E11. Timeseries for average 2 m air temperature (T_{2m}) over domain d03 on cloudy/rainy days during 2012.

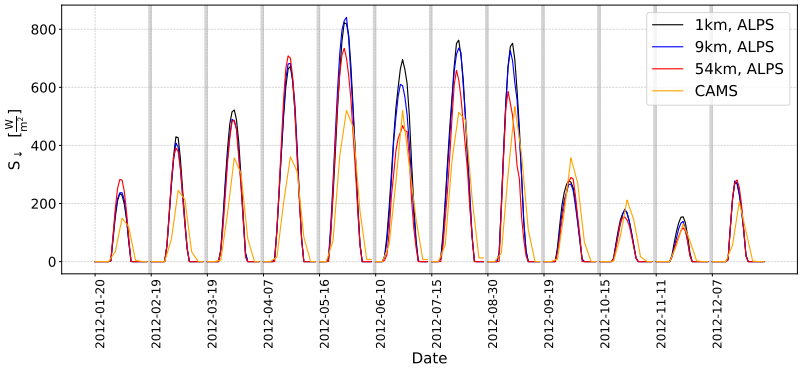

Figure E12. Timeseries for average shortwave downward radiation (S↓) over domain d03 on cloudy/rainy days during 2012.

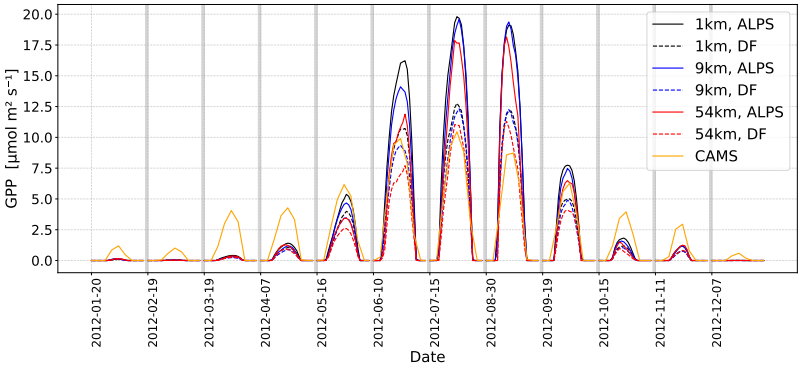

Figure E13. Timeseries for average gross primary production (GPP) over domain d03 on cloudy/rainy days during 2012.

https://doi.org/10.5194/egusphere-2026-939
Preprint. Discussion started: 8 May 2026

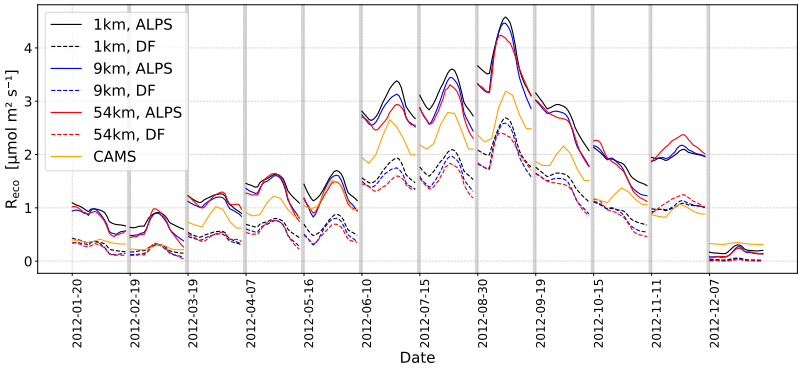

Figure E14. Timeseries for average ecosystem respiration (R_{eco}) over domain d03 on cloudy/rainy days during 2012.

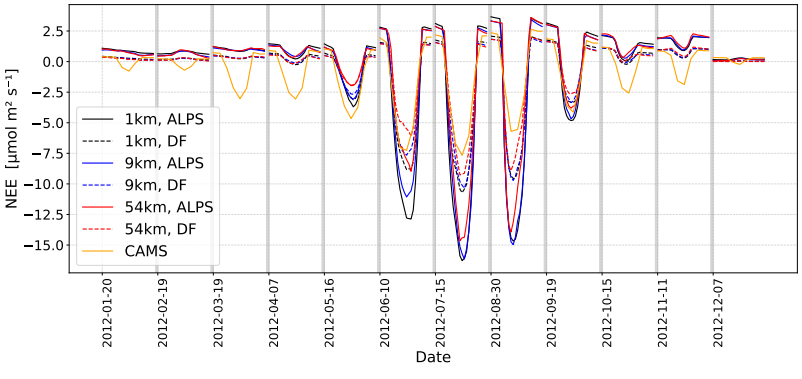

Figure E15. Time series of domain-averaged net ecosystem exchange (NEE) over domain d03 on cloudy/rainy days during 2012.

https://doi.org/10.5194/egusphere-2026-939
Preprint. Discussion started: 8 May 2026

E4 Details on VPRM parameter optimization

This subsection provides technical details and visual comparisons related to VPRM parameter optimization. Figure E16 compares DF, which is used as the initial guess for parameters, and the optimized SITE parameters against measured FLUXNET data for Monte Bondone (IT-MBo) in 2012. Figure E17 shows the final optimized VPRM parameters categorized per PFT and per site ID. Figure E18 presents the Normalized Nash-Sutcliffe Efficiency (NNSE) values achieved by the Alpine-optimized parameters for GPP, R_{eco}, and NEE per PFT.

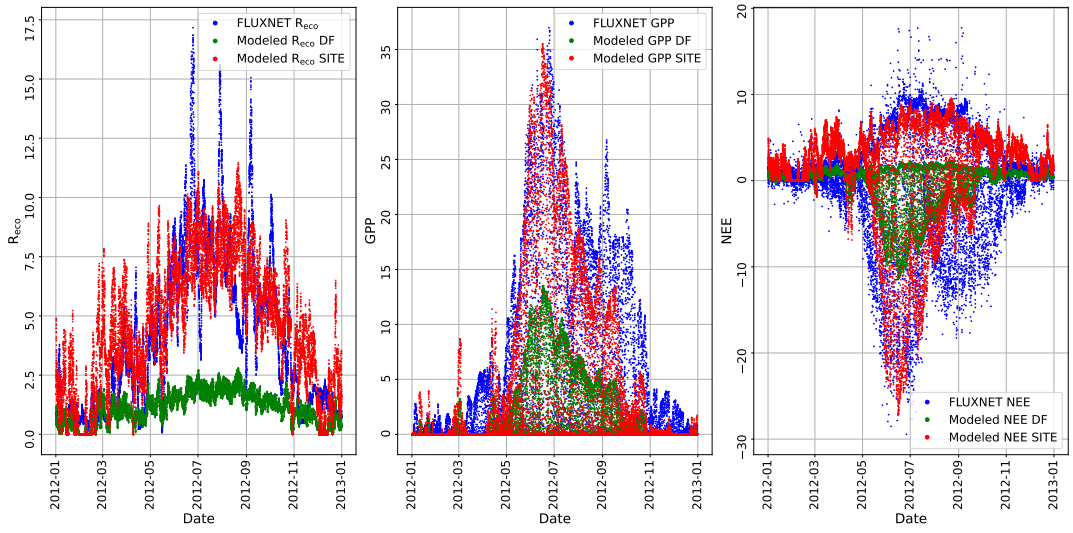

Figure E16. Comparison of measured FLUXNET2015 (blue) R_{eco}, GPP and NEE at Monte Bondone (IT-MBo) in 2012 to DF parameters (green) and the optimized IT-MBo SITE parameters (red), using FLUXNET2015 data to drive VPRM.

https://doi.org/10.5194/egusphere-2026-939
Preprint. Discussion started: 8 May 2026

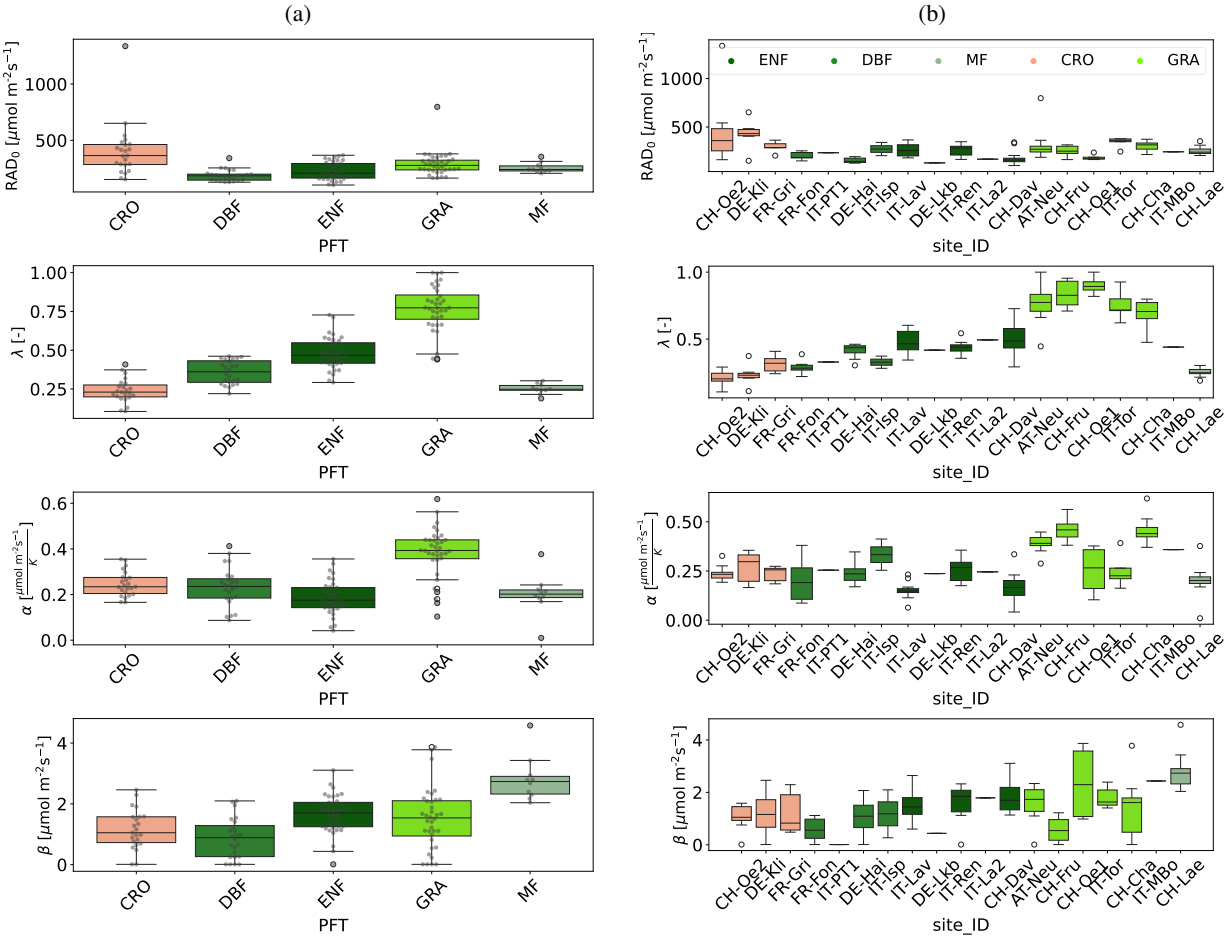

Figure E17. Alpine optimized VPRM parameters per plant functional type (PFT) in panel (a) and per site ID in panel (b).

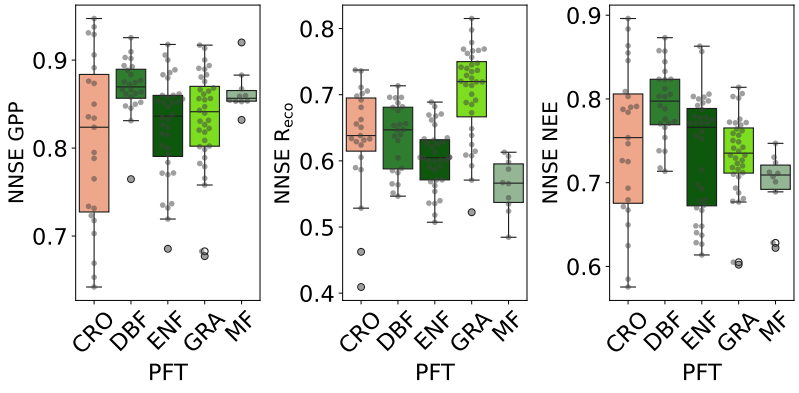

Figure E18. Normalized Nash-Sutcliffe Efficiency (NNSE) values for gross primary production (GPP), ecosystem respiration (Reco), and net ecosystem exchange (NEE) using Alpine optimized parameters for VPRM per plant functional type (PFT).

https://doi.org/10.5194/egusphere-2026-939
Preprint. Discussion started: 8 May 2026

Author contributions. MR conducted the model development, performed the simulations and analysis, and wrote the manuscript. MWR, GW, AG supervised the work and contributed to the discussion and revision of the manuscript.

Competing interests. The authors declare no competing interests.

Disclaimer. Publisher's note:

Acknowledgements. This study was supported by a DOC Fellowship of the Austrian Academy of Sciences awarded to MR. Computational resources were provided by the Austrian Ministry of Science (BMWF) through the Uni Infrastrukturprogramm within the Focal Point Scientific Computing at the University of Innsbruck. We gratefully acknowledge the FLUXNET community for providing the exceptionally useful FLUXNET2015 dataset and thank the principal investigators of the FLUXNET sites used in this study for making their data available. We acknowledge ECMWF for providing the ERA5 reanalysis data and the Copernicus Atmosphere Monitoring Service for the global CO_2 inversion data. This study has utilized MODIS surface reflectance data (MOD09A1, Version 6) for EVI and LSWI, Shuttle Radar Topography Mission elevation data, and CORINE Land Cover 2018 from the European Environment Agency.

https://doi.org/10.5194/egusphere-2026-939
Preprint. Discussion started: 8 May 2026

References

Agustí-Panareda, A., Massart, S., Chevallier, F., Balsamo, G., Boussetta, S., Dutra, E., and Beljaars, A.: A Biogenic CO_2 Flux Adjustment Scheme for the Mitigation of Large-scale Biases in Global Atmospheric CO_2 Analyses and Forecasts, Atmospheric Chemistry and Physics, 16, 10 399–10 418, 2016.

Aubinet, M., Feigenwinter, C., Heinesch, B., Bernhofer, C., Canepa, E., Lindroth, A., Montagnani, L., Rebmann, C., Sedlak, P., and Van Gorsel, E.: Direct advection measurements do not help to solve the night-time CO_2 closure problem: Evidence from three different forests, Agric. For. Meteorol., 150, 655–664, 2010.

Beck, V., Koch, T., Kretschmer, R., Marshall, J., Ahmadov, R., Gerbig, C., Pillai, D., and Heimann, M.: The WRF Greenhouse Gas Model (WRF-GHG). Technical Report No. 25, Tech. rep., Max Planck Institute for Biogeochemistry, Jena, Germany, 2011.

Bonnet, P., Pastori, L., Schwabe, M., Giorgetta, M., Iglesias-Suarez, F., and Eyring, V.: Tuning the ICON-A 2.6. 4 climate model with machine-learning-based emulators and history matching, Geoscientific Model Development, 18, 3681–3706, 2025.

Boussetta, S., Balsamo, G., Beljaars, A., Panareda, A.-A., Calvet, J.-C., Jacobs, C., van den Hurk, B., Viterbo, P., Lafont, S., Dutra, E., et al.: Natural Land Carbon Dioxide Exchanges in the ECMWF Integrated Forecasting System: Implementation and Offline Validation, Journal of Geophysical Research: Atmospheres, 118, 5923–5946, 2013.

Callewaert, S., Brioude, J., Langerock, B., Duflot, V., Fonteyn, D., Müller, J.-F., Metzger, J.-M., Hermans, C., Kumps, N., Ramonet, M., et al.: Analysis of CO 2, CH 4, and CO surface and column concentrations observed at Réunion Island by assessing WRF-Chem simulations, Atmospheric Chemistry and Physics, 22, 7763–7792, 2022.

Cao, J., Wang, R., Chen, J. M., Yang, M., Cheng, Z., and Miao, G.: Quantifying topographic effects on carbon and water fluxes over mountainous areas, Journal of Geophysical Research: Biogeosciences, 130, e2025JG008 878, 2025.

Chandrasekar, K., Sesha Sai, M., Roy, P., and Dwevedi, R.: Land Surface Water Index (LSWI) response to rainfall and NDVI using the MODIS Vegetation Index product, International journal of remote sensing, 31, 3987–4005, 2010.

Chen, F. and Dudhia, J.: Coupling an advanced land surface–hydrology model with the Penn State–NCAR MM5 modeling system. Part I: Model implementation and sensitivity, Monthly weather review, 129, 569–585, 2001.

Chen, J., Gerbig, C., Marshall, J., and Totsche, K. U.: Short-term forecasting of regional biospheric CO 2 fluxes in Europe using a light-use-efficiency model, Geoscientific Model Development Discussions, 2019, 1–26, 2019.

Chen, W., Wang, S., Wang, J., Xia, J., Luo, Y., Yu, G., and Niu, S.: Evidence for widespread thermal optimality of ecosystem respiration, Nature Ecology & Evolution, 7, 1379–1387, 2023.

Custódio, D., Borrego, C., and Relvas, H.: Worldwide Evaluation of CAMS-EGG4 CO2 Data Re-Analysis at the Surface Level, Toxics, 10, 331, 2022.

de Bode, M., Hedde, T., Roubin, P., and Durand, P.: A Method to improve land use representation for weather simulations based on high-resolution data sets—application to corine land cover data in the WRF Model, Earth and Space Science, 10, e2021EA002 123, 2023.

Destro, M., Rotach, M. W., and Lehner, M.: Characterisation of the Surface Energy Balance Residual in Complex Terrain, Boundary-Layer Meteorology, in press, 2026.

European Union's Copernicus Land Monitoring Service information: CORINE Land Cover 2018 (raster 100 m), Europe, 6-yearly [data set], https://doi.org/10.2909/960998c1-1870-4e82-8051-6485205ebbac, 2020.

Fatichi, S., Pappas, C., Zscheischler, J., and Leuzinger, S.: Modelling Carbon Sources and Sinks in Terrestrial Vegetation, New Phytologist, 221, 652–668, 2019.

https://doi.org/10.5194/egusphere-2026-939
Preprint. Discussion started: 8 May 2026

Friedlingstein, P., O'sullivan, M., Jones, M. W., Andrew, R. M., Hauck, J., Olsen, A., Peters, G. P., Peters, W., Pongratz, J., Sitch, S., et al.: Global Carbon Budget 2020, Earth System Science Data, 12, 3269–3340, 2020.

Friend, A. D., ALMUT, A., Y., K. N., Lomas, M., Ogée, J., CHRISTIAN, R., W., R. S., JEAN-DIEGO, S., STEPHEN, S., NICOLAS, V., F., W. I., and SÖNKE, Z.: FLUXNET and modelling the global carbon cycle, Glob. Change Biol., 13, 610–633, 2007.

Gerbig, C.: Parameters for the Vegetation Photosynthesis and Respiration Model VPRM, ICOS-ERIC - Carbon Portal [data set], https://doi.org/10.18160/HF4C-G0KK, 2024.

Glauch, T., Marshall, J., Gerbig, C., Botía, S., Gałkowski, M., Vardag, S. N., and Butz, A.: pyVPRM: A next-generation Vegetation Photosynthesis and Respiration Model for the post-MODIS era, Geoscientific Model Development, 18, 4713–4742, 2025.

Gommers, R., Virtanen, P., Haberland, M., Burovski, E., Reddy, T., Weckesser, W., Oliphant, T. E., Cournapeau, D., Nelson, A., Roy, P., et al.: scipy/scipy: SciPy, https://doi.org/10.5281/zenodo.595738, 2024.

Gourdji, S. M., Karion, A., Lopez-Coto, I., Ghosh, S., Mueller, K. L., Zhou, Y., Williams, C. A., Baker, I. T., Haynes, K. D., and Whetstone, J. R.: A modified Vegetation Photosynthesis and Respiration Model (VPRM) for the eastern USA and Canada, evaluated with comparison to atmospheric observations and other biospheric models, Journal of Geophysical Research: Biogeosciences, 127, e2021JG006 290, 2022.

Groenendijk, M., Dolman, A., Van der Molen, M., Leuning, R., Arneth, A., Delpierre, N., Gash, J., Lindroth, A., Richardson, A., Verbeeck, H., et al.: Assessing Parameter Variability in a Photosynthesis Model within and between Plant Functional Types using global Fluxnet Eddy Covariance Data, Agricultural and forest meteorology, 151, 22–38, 2011.

Hersbach, H., Bell, B., Berrisford, P., Biavati, G., Horányi, A., J., M. S., Nicolas, J., Peubey, C., Radu, R., Rozum, I., Schepers, D., Simmons, A., Soci, C., Dee, D., and Thépaut, J.-N.: ERA5 hourly data on single levels from 1940 to present, Copernicus Climate Change Service, Climate Data Store [data set], https://doi.org/10.24381/cds.adbb2d47, 2023.

Hogan, R. J. and Bozzo, A.: A flexible and efficient radiation scheme for the ECMWF model, Journal of Advances in Modeling Earth Systems, 10, 1990–2008, 2018.

Hu, X.-M., Crowell, S., Wang, Q., Zhang, Y., Davis, K. J., Xue, M., Xiao, X., Moore, B., Wu, X., Choi, Y., et al.: Dynamical downscaling of CO2 in 2016 over the contiguous United States using WRF-VPRM, a weather-biosphere-online-coupled model, Journal of Advances in Modeling Earth Systems, 12, e2019MS001 875, 2020.

Hu, Z., Sun, S., Sun, X., Lin, S., Song, C., and Wang, G.: Controlling factors of the spatial-temporal fluctuations in evapotranspiration along an elevation gradient across humid montane ecosystems, Water Resources Research, 59, e2022WR033 228, 2023.

Huggannavar, V. and Indu, J.: Coupled weather-biosphere model (WRF-VPRM) response to extreme land cover scenarios over Ganga basin: a cross-component analysis, Environmental Research Communications, 5, 085 006, 2023.

Igarashi, Y., Katul, G. G., Kumagai, T., Yoshifuji, N., Sato, T., Tanaka, N., Tanaka, K., Fujinami, H., Suzuki, M., and Tantasirin, C.: Separating physical and biological controls on long-term evapotranspiration fluctuations in a tropical deciduous forest subjected to monsoonal rainfall, Journal of Geophysical Research: Biogeosciences, 120, 1262–1278, 2015.

Inness, A., Ades, M., Agustí-Panareda, A., Barré, J., Benedictow, A., Blechschmidt, A.-M., Dominguez, J. J., Engelen, R., Eskes, H., Flemming, J., et al.: The CAMS reanalysis of atmospheric composition, Atmospheric Chemistry and Physics, 19, 3515–3556, 2019.

Jose, R. S., Perez-Camanyo, J. L., and Jimenez-Gañan, M.: Assessing future greenhouse gas concentrations in Madrid, Spain: a dynamical downscaling approach using WRF-VPRM, Air Quality, Atmosphere & Health, pp. 1–11, 2025.

JPL, N.: NASA Shuttle Radar Topography Mission Global 3 arc second number NetCDF, NASA EOSDIS Land Processes Distributed Active Archive Center (DAAC) [data set], 2013.

https://doi.org/10.5194/egusphere-2026-939
Preprint. Discussion started: 8 May 2026

Kattge, J. and Knorr, W.: Temperature acclimation in a biochemical model of photosynthesis: a reanalysis of data from 36 species, Plant, cell & environment, 30, 1176–1190, 2007.

Li, D., Bou-Zeid, E., Barlage, M., Chen, F., and Smith, J. A.: Development and evaluation of a mosaic approach in the WRF-Noah framework, Journal of Geophysical Research: Atmospheres, 118, 11–918, 2013.

Li, X., Hu, X.-M., Cai, C., Jia, Q., Zhang, Y., Liu, J., Xue, M., Xu, J., Wen, R., and Crowell, S. M.: Terrestrial CO2 fluxes, concentrations, sources and budget in Northeast China: Observational and modeling studies, Journal of Geophysical Research: Atmospheres, 125, e2019JD031 686, 2020.

Liu, Y.: Optimum Temperature for Photosynthesis: from Leaf to Ecosystem-Scale, Science Bulletin, 65, 601–604, 2020.

Mahadevan, P., Wofsy, S. C., Matross, D. M., Xiao, X., Dunn, A. L., Lin, J. C., Gerbig, C., Munger, J. W., Chow, V. Y., and Gottlieb, E. W.: A satellite-based biosphere parameterization for net ecosystem CO2 exchange: Vegetation Photosynthesis and Respiration Model (VPRM), Global Biogeochemical Cycles, 22, 2008.

Marbaix, P., Gallée, H., Brasseur, O., and van Ypersele, J.-P.: Lateral boundary conditions in regional climate models: a detailed study of the relaxation procedure, Monthly weather review, 131, 461–479, 2003.

Mengoli, G., Agustí-Panareda, A., Boussetta, S., Harrison, S. P., Trotta, C., and Prentice, I. C.: Ecosystem photosynthesis in land-surface models: a first-principles approach incorporating acclimation, Journal of Advances in Modeling Earth Systems, 14, e2021MS002 767, 2022.

Mengoli, G., Harrison, S. P., and Prentice, I. C.: The response of carbon uptake to soil moisture stress: adaptation to climatic aridity, Global Change Biology, 31, e70 098, 2025.

Morcrette, J.-J.: On the effects of the temporal and spatial sampling of radiation fields on the ECMWF forecasts and analyses, Monthly weather review, 128, 876–887, 2000.

Parazoo, N. C., Coleman, R. W., Yadav, V., Stavros, E. N., Hulley, G., and Hutyra, L.: Diverse biosphere influence on carbon and heat in mixed urban Mediterranean landscape revealed by high resolution thermal and optical remote sensing, Science of The Total Environment, 806, 151 335, 2022.

Park, C., Park, S.-Y., Gurney, K. R., Gerbig, C., DiGangi, J. P., Choi, Y., and Lee, H. W.: Numerical simulation of atmospheric CO2 concentration and flux over the Korean Peninsula using WRF-VPRM model during Korus-AQ 2016 campaign, PLoS One, 15, e0228 106, 2020.

Pastorello, G., Trotta, C., Canfora, E., Chu, H., Christianson, D., Cheah, Y.-W., Poindexter, C., Chen, J., Elbashandy, A., Humphrey, M., et al.: The FLUXNET2015 dataset and the ONEFlux processing pipeline for eddy covariance data, Scientific data, 7, 225, 2020.

Penrose, R.: A generalized inverse for matrices, in: Mathematical proceedings of the Cambridge philosophical society, vol. 51, pp. 406–413, Cambridge University Press, 1955.

Platter, A., Scholz, K., Hammerle, A., Rotach, M. W., and Wohlfahrt, G.: Agreement of multiple night- and daytime filtering approaches of eddy covariance-derived net ecosystem CO2 exchange over a mountain forest, Agricultural and Forest Meteorology, 356, 110 173, 2024.

Prein, A. F., Langhans, W., Fosser, G., Ferrone, A., Ban, N., Goergen, K., Keller, M., Tölle, M., Gutjahr, O., Feser, F., et al.: A review on regional convection-permitting climate modeling: Demonstrations, prospects, and challenges, Reviews of geophysics, 53, 323–361, 2015.

Raju, A., Sijikumar, S., Burman, P. K. D., Valsala, V., Tiwari, Y. K., Mukherjee, S., Lohani, P., and Kumar, K.: Very High-Resolution Net Ecosystem Exchange over India Using Vegetation Photosynthesis and Respiration Model (VPRM) Simulations, Ecological Modelling, 481, 110 340, 2023.

https://doi.org/10.5194/egusphere-2026-939
Preprint. Discussion started: 8 May 2026

Ranit, Bao, S., Koirala, S., Brenning, A., Reichstein, M., Tagesson, T., Liddell, M., Ibrom, A., Wolf, S., Šigut, L., et al.: Addressing challenges in simulating inter–annual variability of gross primary production, Journal of Advances in Modeling Earth Systems, 17, e2024MS004 697, 2025.

Reif, M.: WRF-VPRM Simulations in Complex Topography: Model Configuration and Sample Output Data, Zenodo [data set], https://doi.org/10.5281/zenodo.18481850, 2026.

Reif, M., Rotach, M. W., Gohm, A., and Wohlfahrt, G.: Carbon dioxide exchange in an idealized valley, Environmental Modelling & Software, 171, 105 887, 2024.

Rotach, M., Wohlfahrt, G., Hansel, A., Reif, M., Wagner, J., and Gohm, A.: The World is Not Flat: Implications for the Global Carbon Balance, Bulletin of the American Meteorological Society, 95, 1021–1028, 2014.

Rotach, M. W., Serafin, S., Ward, H. C., Arpagaus, M., Colfescu, I., Cuxart, J., De Wekker, S. F., Grubišic, V., Kalthoff, N., Karl, T., et al.: A collaborative effort to better understand, measure, and model atmospheric exchange processes over mountains, Bulletin of the American Meteorological Society, 103, E1282–E1295, 2022.

Segura-Barrero, R., Lauvaux, T., Lian, J., Ciais, P., Badia, A., Ventura, S., Bazzi, H., Abbessi, E., Fu, Z., Xiao, J., et al.: Heat and drought events alter biogenic capacity to balance CO2 budget in south-western Europe, Global Biogeochemical Cycles, 39, e2024GB008 163, 2025.

Simonet, G., Rotach, M. W., and Lehner, M.: Physically consistent mesoscale model evaluation in complex terrain, Quarterly Journal of the Royal Meteorological Society, p. e70063, 2025.

Stocker, B. D., Wang, H., Smith, N. G., Harrison, S. P., Keenan, T. F., Sandoval, D., Davis, T., and Prentice, I. C.: P-model v1. 0: an optimality-based light use efficiency model for simulating ecosystem gross primary production, Geoscientific Model Development, 13, 1545–1581, 2020.

Storn, R. and Price, K.: Differential evolution–a simple and efficient heuristic for global optimization over continuous spaces, Journal of global optimization, 11, 341–359, 1997.

Tarantola, A.: Inverse problem theory and methods for model parameter estimation, SIAM, 2005.

Wagner, J. S., Gohm, A., and Rotach, M. W.: The Impact of Horizontal Model Grid Resolution on the Boundary Layer Structure over an Idealized Valley, Monthly Weather Review, 142, 3446–3465, 2014a.

Wagner, J. S., Gohm, A., and Rotach, M. W.: The impact of horizontal model grid resolution on the boundary layer structure over an idealized valley, Monthly Weather Review, 142, 3446–3465, 2014b.

Walker, A. P., De Kauwe, M. G., Bastos, A., Belmecheri, S., Georgiou, K., Keeling, R. F., McMahon, S. M., Medlyn, B. E., Moore, D. J., Norby, R. J., et al.: Integrating the Evidence for a Terrestrial Carbon Sink caused by increasing Atmospheric CO_2, New Phytologist, 229, 2413–2445, 2021.

Wang, H., Prentice, I. C., Davis, T. W., Keenan, T. F., Wright, I. J., and Peng, C.: Photosynthetic responses to altitude: an explanation based on optimality principles, New Phytologist, 213, 976–982, 2017a.

Wang, H., Prentice, I. C., Keenan, T. F., Davis, T. W., Wright, I. J., Cornwell, W. K., Evans, B. J., and Peng, C.: Towards a universal model for carbon dioxide uptake by plants, Nature plants, 3, 734–741, 2017b.

Woude, A. M., De Kok, R., Smith, N., Luijkx, I. T., Botía, S., Karstens, U., Kooijmans, L. M., Koren, G., Meijer, H. A., Steeneveld, G.-J., et al.: Near-real-time CO 2 fluxes from CarbonTracker Europe for high-resolution atmospheric modeling, Earth System Science Data, 15, 579–605, 2023.

https://doi.org/10.5194/egusphere-2026-939
Preprint. Discussion started: 8 May 2026

Xiao, Z., Liang, S., Wang, J., Jiang, B., and Li, X.: Real-time retrieval of Leaf Area Index from MODIS time series data, Remote Sensing of Environment, 115, 97–106, 2011.

Zaehle, S. and Dalmonech, D.: Carbon–nitrogen interactions on land at global scales: current understanding in modelling climate biosphere feedbacks, Curr. Opin. Environ. Sustainability, 3, 311 – 320, 2011.

Zhao, X., Chen, J., Marshall, J., Hachinger, S., Dietrich, F., Shekhar, A., Gensheimer, J., Wenzel, A., Gerbig, C., et al.: Understanding greenhouse gas (GHG) column concentrations in Munich using the Weather Research and Forecasting (WRF) model, Atmospheric Chemistry and Physics, 23, 14 325–14 347, 2023.